



# Modeling multi-scale processes in hydraulic fracture propagation using the implicit level set algorithm

A. Peirce\*

*Department of Mathematics, University of British Columbia, Vancouver, British Columbia, V6T 1Z2, Canada*

Received 2 May 2014; accepted 22 August 2014

Available online 28 September 2014

---

## Highlights

- We develop an ILSA scheme to model multi-scale behavior in planar hydraulic fractures.
- The multiscale ILSA scheme shows close agreement with published radial solutions.
- The multiscale ILSA scheme provides reference solutions for an HF in a symmetric stress jump.
- The ILSA solutions are used to calibrate P3D models.

---

## Abstract

In this paper we describe an implicit level set algorithm (ILSA) (Peirce and Detournay, 2008) suitable for modeling multi-scale behavior in planar hydraulic fractures propagating in three dimensional elastic media. This multi-scale behavior is typically encountered when multiple physical processes compete to determine the location of the fracture free boundary. Instead of having to match the mesh size to the finest active length scale, or having to re-mesh as the dominant length scales change in space and time, the novel ILSA scheme is able to represent the required multi-scale behavior on a relatively coarse rectangular mesh. This is achieved by using the local front velocity to construct, for each point of a set of control points, a mapping that adaptively identifies the dominant length scale at which the appropriate multi-scale universal asymptotic solution needs to be sampled. Finer-scale behavior is captured in a weak sense by integrating the universal asymptotic solution for the fracture width over partially filled tip elements and using these integrals to set the average values of the widths in all tip elements. The ILSA solution shows good agreement with a multi-scale reference solution comprising a radial solution that transitions from viscosity to toughness dominated propagation regimes. The ILSA scheme is also used to model blade-like hydraulic fractures that break through stress barriers located symmetrically with respect to the injection point. For the zero toughness case, the ILSA solution shows close agreement to experimental results. The multi-scale ILSA scheme is also used to provide results when the material toughness  $K_{IC}$  is non-zero. In this case different parts of the fracture-free-boundary can be propagating in different regimes. It is hoped that the multi-scale ILSA solutions presented here will form a set of reference results that can be used to benchmark simulators that use a propagation criterion based on only one dissipative process (either toughness or viscosity). The multi-scale ILSA solutions at larger times (for which plane strain conditions develop in vertical cross sections) are compared with and show close agreement to plane strain exact solutions for height-growth and the fracture width in vertical cross sections. This comparison provides some measure of the

---

\* Tel.: +1 6042224435.

E-mail addresses: [anthony.peirce@gmail.com](mailto:anthony.peirce@gmail.com), [peirce@math.ubc.ca](mailto:peirce@math.ubc.ca).

accuracy of the multi-scale ILSA scheme. The multi-scale ILSA solutions are also used to identify the regimes of applicability of pseudo 3D (P3D) approximate solutions. These ILSA solutions can also be used to design improved P3D models.

© 2014 Elsevier B.V. All rights reserved.

*Keywords:* Hydraulic fracture; Level set methods; Multi-scale phenomena; Stress jumps; P3D models

---

## 1. Introduction

Hydraulic fractures (HF) are a class of brittle fractures that propagate in pre-stressed solid media due to the injection of a viscous fluid. In the oil and gas industry HF have, for some time, been deliberately created in reservoirs to enhance the recovery of hydrocarbons by the creation of permeable pathways [1]. The application of HF in geotechnical engineering is growing. For example, in the mining industry HF have been used to weaken the rock and enhance the so-called block-caving process [2,3]. Similarly, the extraction of geothermal energy requires the creation of new fractures to increase existing fracture networks. Hydraulic fractures have also been used for waste disposal and are likely to play a key role in the gravitational trapping of CO<sub>2</sub> in deep, low permeability, ocean sediments. The propagation of hydraulic fractures into undesirable locations can have severe safety consequences in the mining industry, and can cause considerable loss of hydrocarbons and environmental damage in the oil industry. Likewise, the perforation of the caprock by HF can reverse the costly capture process involved in CO<sub>2</sub> sequestration. It is therefore of considerable importance to have accurate models in order to be able to predict the advance of HF to achieve an effective design of the engineering parameters in the injection process.

Mathematical models of HF involve a degenerate system of hyper-singular integro-partial differential equations defined on a domain with a moving boundary [4]. This class of problem has been shown to exhibit a multi-scale structure [5] in which the fracture can propagate in a number of different modes each determined by the dominant physical process active at the tip of the fracture. A number of studies on the propagation of HF in the special case of plane strain have clearly established the pivotal role of the asymptotic behavior of the solution in the vicinity of the fracture tip [6,7,5,8–10]. The tip behavior of HF propagating in a state of plane strain is also important for the analysis of planar HF in 3D elastic media. Indeed, in the vicinity of the perimeter of such a planar HF, the governing equations can be shown [11] to reduce to those of an HF propagating in a state of plane strain—provided the boundary of the fracture is smooth. In that paper, the plane strain asymptotic solutions were combined with an implicit level set algorithm (ILSA) to locate the HF free boundary to achieve remarkably accurate results with relatively modest computational resources [12]. The ILSA approach developed in [11] was restricted to modeling propagating HF in which it is assumed that a single physical process is active in determining the progress of the fracture. In this case, one of the corresponding asymptotic solutions is used at the computational length scale to locate the free boundary.

However, more than one and sometimes multiple physical processes are often active in determining the progress of a propagating HF [5]. In this case, multiple length scales, each associated with a different physical process, can be active in determining the location of the free boundary. If one of the physical processes is dominant, then the length scale associated with that process should be matched to the computational length scale or mesh size. It is also possible for the dominant physical process to change from one to another as the HF evolves by passing through an intermediate regime in which both physical processes contribute equally to the location of the HF free boundary. In this case, the computational length scale needs to be adapted to match the dominant physical process active at that time. Moreover, if heterogeneities in the rock are present, then it is possible for the propagation of different parts of the fracture boundary to be simultaneously dominated by different physical processes. In this case, the computational length scale needs to be adapted in space and time to match to the length scale associated with the dominant physical process active locally. Thus the big challenge is to devise a numerical model that can capture such heterogeneous, time-dependent, multi-scale processes. One approach would be to fix the mesh size to the finest length scale active in the problem. Unfortunately, since the multi-scale behavior typically ranges over 6–8 orders of magnitude (see [11]) the computational cost of this option would be prohibitive. Another option would be to adapt the mesh size in space and time to match the dominant physical process active at each location along the front. However, this would also be an extremely complex approach to implement.

The objective of this paper is to adapt the ILSA approach to arrive at an efficient scheme that can capture this multi-scale behavior using a relatively coarse mesh. We use a fixed mesh of rectangular elements and locate the free

boundary using a universal asymptotic solution [13] for a semi infinite fracture propagating with a constant speed  $V$  in an infinite elastic medium under conditions of plane strain. This free boundary location is implemented adaptively at each control point along the fracture boundary by constructing a map, which is a function of the local front velocity, to identify the appropriate length scale at which to sample the universal asymptotic solution in order to capture the dominant physical process currently active at that control point. Once the dominant length scale has been identified, all the finer-scale structure of the multi-scale solution is captured *in a weak sense*, by using the universal asymptotic solution to calculate the fluid volume contained in each tip element. These asymptotic tip volumes are then used to assign the average crack opening in all the tip elements. Having set the dominant physical length scale to match the mesh size, and captured the finer-scale structure in a weak sense, naturally the algorithm is also able to capture the applicable coarser-scale processes active in the problem. Thus the novel ILSA approach provides an approximate scheme that accounts for all the multi-scale behavior active in the HF propagation problem.

We test the novel algorithm against a reference solution [14] for a radially symmetric crack in which the two physical processes of viscous dissipation (dependent on the fluid viscosity) and energy release due to fracturing (dependent on the fracture toughness) are both active. Though both of these the two dissipative processes are present, it can be shown that such radial fractures initially propagate in a regime in which viscosity dominates the propagation process, and, as the fracture evolves, the fracture toughness becomes more important and ultimately dominates the propagation process. We also demonstrate the performance of the new algorithm in a heterogeneous situation in which different parts of the fracture boundary propagate at different speeds that are associated with different physical processes. We consider a hydraulic fracture that starts off radially symmetric and which is subsequently deformed into a blade-like geometry when it encounters positive jumps in the confining stress field that are situated symmetrically about the injection point. One of the key questions in hydraulic fracture treatments is the extent to which an evolving hydraulic fracture will penetrate beyond the interface across which such a stress jump occurs. Until the recent ground-breaking stress jump experiment [15], this was largely an open question. These experiments can only feasibly be performed between two de-bonded surfaces, so they only provide benchmark height growth solutions when the fracture is propagating in the viscosity dominated regime. What happens when the toughness is relatively small so that there is a competition between viscous and toughness driven dissipative processes? The ILSA algorithm can be used to model this situation since it is able to capture the multi-scale tip behavior and to autonomously adjust the relative weight of the competing processes of viscous dissipation and energy release due to fracturing. It is therefore possible to extend the viscosity dominated experimental results to include the intermediate regimes in which both these physical processes compete. Thus the extension from viscosity dominated propagation through the intermediate regime, in which both processes compete, into the toughness dominated regime provides a set of useful benchmark results. These benchmarks can, for example, be used to validate numerical simulators that rely on a single propagation criterion (associated with viscosity or toughness dominated propagation) to advance the front. As the blade-like fractures become more elongated, a state of plane strain starts to develop in vertical cross sections of the fracture sampled away from the lateral fracture tips, and fluid pressure field can be seen to vary very little in such vertical cross sections. Assuming that a situation of plane strain prevails for any vertical cross-section, it is possible to obtain an exact expression for the fracture opening profile [16] as well as the height growth  $h$ —given the fracture toughness and the pressure [17]. Indeed these assumptions and solutions are fundamental to the so-called pseudo 3D (P3D) models [18, 19,16], which are widely used to design hydraulic fracture treatments in the oil and gas industry. We use these exact plane strain solutions to test the new ILSA algorithm for sufficiently large times for the plane strain approximation to be reasonably accurate. Conversely, we also use the ILSA solution to test the range of applicability of the P3D models.

In Section 2, we state the governing equations for a planar hydraulic fracture propagating in an infinite, homogeneous linearly elastic medium; in Section 3, we introduce characteristic scalings for the variables of the problem, establish the viscous, toughness, and viscosity–toughness scalings associated with viscosity dominated, toughness dominated, and transition regimes, respectively; we also state the governing equations for a semi infinite fracture propagating with a constant velocity under conditions of plane strain, introduce the appropriate scaling, and derive the fundamental mapping between the semi infinite fracture and the finite fracture; in Section 4 we describe the implementation of the generalized asymptote in the implicit level set algorithm, including a brief description of the discretization procedure, the implicit level set algorithm, the procedure used to determine the crack volume in tip elements by integrating the generalized asymptote; in Section 5 we present the numerical results in which the new ILSA solution is compared to a reference radial solution as well as an example of a hydraulic fracture propagating in a heterogeneous geological stress field in which the propagation of different parts of the perimeter are dominated by

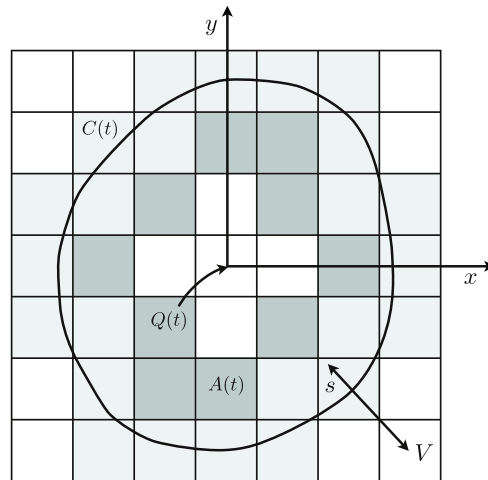


Fig. 1. Planar fracture with a footprint  $A(t)$  inscribed within the curve  $C(t)$  moving with the normal velocity  $V$ . The  $x$ - $y$  coordinate system is centered on the point source.

different physical processes; this solution is compared with experiments and solutions from a P3D model; in Section 6 we provide some concluding remarks.

## 2. Mathematical model

### 2.1. Assumptions

The equations governing the propagation of a hydraulic fracture in a reservoir have to account for the dominant physical processes taking place during the treatment, namely the deformation of the rock, the creation of new fracture surfaces, the flow of the fracturing fluid in the crack, the leak-off of the fracturing fluid into the reservoir, and the formation of a cake by particles in the fluid. Besides the standard assumptions regarding the applicability of linear elastic fracture mechanics (LEFM) and lubrication theory, we make a series of simplifications that can readily be justified for the purposes of this contribution: (i) the rock is homogeneous and impermeable (toughness  $K_{Ic}$ , Young's modulus  $E$ , and Poisson's ratio  $\nu$  thus all have uniform values), (ii) the fracturing fluid is incompressible and Newtonian (with a dynamic viscosity  $\mu$ ), (iii) the fracture is always in limit equilibrium, (iv) gravity is neglected in the lubrication equation, and (v) the fluid front coincides with the crack front, because the lag between the two fronts is negligible under typical high confinement conditions encountered in reservoir stimulation [20–22].

We have assumed that the rock is impermeable to enable us to focus on the treatment of the multi-scale behavior when only the two competing dissipative processes of viscosity and toughness are involved. Incorporating leak-off using the framework that we describe proceeds in an entirely analogous manner by incorporating the appropriate leak-off storage asymptotics. Note that the assumption that  $K_{Ic}$  and  $\mu$  are homogeneous can be relaxed without any significant changes to the model. The assumption that  $E$  and  $\nu$  are homogeneous is not trivial to relax (see for example [23–25]), however we do assume a rectangular Eulerian grid on which an efficient multi-layer algorithm can be implemented without revising the algorithm presented in this paper by merely replacing the Green's function matrix elements for a homogeneous elastic medium by those for a layered elastic medium.

### 2.2. Governing equations

The solution of the hydraulic fracture problem comprises the fracture aperture  $w(x, y, t)$ , the fluid pressure  $p_f(x, y, t)$ , the fluid flux  $\mathbf{q}(x, y, t)$ , and the position of the front  $C(t)$ , where  $t$  denotes the time and  $x, y$  are the coordinates in a system of axes referenced to the injection point (see Fig. 1). The solution depends on the injection rate  $Q(t)$ , the far-field compressive stress  $\sigma(x, y)$  perpendicular to the fracture plane (a known function of position), and the three material parameters  $\mu', E', K'$  defined as

$$\mu' = 12\mu, \quad E' = \frac{E}{1 - \nu^2}, \quad K' = 4 \left( \frac{2}{\pi} \right)^{1/2} K_{Ic}. \quad (2.1)$$

Here  $E'$  is the plane strain modulus, and the alternate viscosity  $\mu'$  and toughness  $K'$  are introduced to keep equations uncluttered by numerical factors. The front  $C(t)$ , and the field quantities  $w(x, y, t)$ ,  $p_f(x, y, t)$ , and  $\mathbf{q}(x, y, t)$  are governed by a set of equations arising from linear elastic fracture mechanics, lubrication theory, and the associated boundary conditions.

2.2.1. Elasticity

In view of the homogeneous (elastic) nature of the infinite medium, the elasticity equations relating the displacement and stress field in the solid can be condensed into a hypersingular integral equation between the fracture aperture  $w$  and the fluid pressure  $p_f$  [26,27]

$$p(x, y, t) = p_f - \sigma = -\frac{E'}{8\pi} \int_{A(t)} \frac{w(x', y', t) dx' dy'}{[(x' - x)^2 + (y' - y)^2]^{3/2}} \tag{2.2}$$

where  $A(t)$  denotes the fracture footprint enclosed by the crack front  $C(t)$  and having a characteristic dimension  $L(t)$ ,  $\sigma(x, y)$  is the prescribed *in-situ* stress field, and  $p$  is the net pressure.

2.2.2. Lubrication

The lubrication equations consist of Poiseuille’s law

$$\mathbf{q} = -\frac{w^3}{\mu'} \nabla p_f \tag{2.3}$$

and the continuity equation

$$\frac{\partial w}{\partial t} + \nabla \cdot \mathbf{q} = Q(t)\delta(x, y). \tag{2.4}$$

Eqs. (2.3)–(2.4) can be combined to yield the Reynolds equation

$$\frac{\partial w}{\partial t} = \frac{1}{\mu'} \nabla \cdot (w^3 \nabla p_f) + Q(t)\delta(x, y). \tag{2.5}$$

2.2.3. Boundary conditions at the moving front  $C(t)$

We consider the singular case in which the fluid front within the fracture and the fracture front coalesce so there is no fluid-lag. In this case [22], the boundary conditions at the front  $C(t)$  are deduced from the propagation criterion, a zero width, and a zero flux condition. Assuming that the fracture is always in limit equilibrium and that a limiting condition is reached everywhere along the front, implies that the fracture aperture in the immediate vicinity of the front is given by

$$w \sim \frac{K'}{E'} s^{1/2} \tag{2.6}$$

where  $s$  denotes the distance from the crack front  $C(t)$  (with the  $s$ -axis directed inwards as shown in Fig. 1). The form of this condition is a classical result of LEFM [28].

The second condition simply expresses a zero flux boundary condition at the fracture tip

$$\lim_{s \rightarrow 0} w^3 \frac{\partial p_f}{\partial s} = 0. \tag{2.7}$$

We note that the pressure gradient becomes infinite as  $s \rightarrow 0$  according to the Reynolds equation (2.5), since  $w \rightarrow 0$  as  $s \rightarrow 0$ . Unlike a classical Stefan boundary condition at a moving front, where the front velocity is given in terms of quantities having a definite limit at the front, the front velocity has to be extracted from an asymptotic analysis of the non-linear system of equations (2.2)–(2.7). For an impermeable medium, the front velocity  $v$  is equal to the average fluid velocity as  $s \rightarrow 0$

$$v = \frac{1}{\mu'} \lim_{s \rightarrow 0} w^2 \frac{\partial p_f}{\partial s} \tag{2.8}$$

which shows that  $v$  is the limit of an indeterminate form. For a permeable medium, this limit can be finite or tend to infinity depending on the tip asymptote [22]. It is therefore clear that front location algorithms, based on knowing the front velocity  $v$ , face a serious challenge due to the need to evaluate large pressure gradients and large leak-off velocities in order to estimate the front velocity.

### 3. Propagation regimes, scaling, and tip asymptotics

#### 3.1. Viscous, toughness and viscosity–toughness scaling

The approach adopted in this section follows the work of [13,20,5,29,11,30]. We introduce a characteristic length scale  $l_*$ , a characteristic time scale  $t_*$ , a characteristic fracture aperture  $w_*$ , and a characteristic (net) pressure  $p_*$  (all yet to be defined). Assuming a nominally radially symmetric fracture, the physical quantities of the problem are thus formally expressed as

$$x = l_*\chi, \quad y = l_*\zeta, \quad t = t_*\tau, \quad w = w_*\Omega, \quad p_f = p_*\Pi_f. \quad (3.1)$$

Furthermore, in order to scale the equations, we introduce the characteristic injection rate  $Q_o$  and the characteristic stress  $\sigma_o$  such that

$$Q = Q_o\psi(\tau), \quad \sigma = \sigma_o\varphi(\chi, \zeta) \quad (3.2)$$

where  $\psi(\tau)$  and  $\varphi(\chi, \zeta)$  are known functions, which we have already chosen to express in terms of the dimensionless time  $\tau$  and space variables  $\chi$  and  $\zeta$ . Since the  $x$  and  $y$  coordinates are both scaled by  $l_*$ , this scaling is particularly pertinent for a radial fracture in which the fracture radius  $R(t)$  is given by  $R(t) = l_*\gamma(\tau)$ .

In the scaled coordinates, the governing equations transform to the following:

$$\Pi(\chi, \zeta, \tau) = \Pi_f(\chi, \zeta, \tau) - \Sigma_o\varphi(\chi, \zeta) = -\frac{\mathcal{G}_e}{8\pi} \int_{\mathcal{A}(\tau)} \frac{\Omega(\chi', \zeta', \tau) d\chi' d\zeta'}{[(\chi' - \chi)^2 + (\zeta' - \zeta)^2]^{3/2}} \quad (3.3)$$

$$\frac{\partial \Omega}{\partial \tau} = \frac{1}{\mathcal{G}_m} \nabla \cdot (\Omega^3 \nabla \Pi_f) + \mathcal{G}_v \psi(\tau) \delta(\chi, \zeta) \quad (3.4)$$

$$\lim_{\xi \rightarrow 0} \frac{\Omega}{\xi^{1/2}} = \mathcal{G}_k, \quad \lim_{\xi \rightarrow 0} \Omega^3 \frac{\partial \Pi_f}{\partial \xi} = 0 \quad (3.5)$$

where  $\Sigma_o$  is the scaled far-field stress field  $\sigma_o/p_*$ ,  $\Pi$  is the net pressure, and  $\mathcal{A}(\tau)$  and  $\mathcal{C}(\tau)$  are respectively the scaled fracture footprint region and boundary curve, and  $\xi = l_*s$  is the scaled normal distance to the scaled boundary curve  $\mathcal{C}(\tau)$ . In (3.3)–(3.5) the dimensionless quantities  $\mathcal{G}_j$  are defined as follows:

$$\mathcal{G}_e = \frac{E'w_*}{p_*l_*}, \quad \mathcal{G}_v = \frac{Q_0t_*}{w_*l_*^2}, \quad \mathcal{G}_m = \frac{\mu' l_*^2}{w_*^2 p_* t_*}, \quad \mathcal{G}_k = \frac{K' l_*^{1/2}}{E'w_*}. \quad (3.6)$$

##### 3.1.1. Viscosity dominated propagation

The scaling for the viscous propagation regime can be obtained by requiring that  $\mathcal{G}_e = \mathcal{G}_v = \mathcal{G}_m = 1$ , from which we obtain the following power law relationships between the viscous length scale  $l_m$ , the width scale  $w_m$ , and the pressure scale  $p_m$  as functions of the characteristic time  $t_*$ :

$$l_m = \left( \frac{E'Q_0^3}{\mu'} \right)^{1/9} t_*^{4/9}, \quad w_m = \left( \frac{\mu'^2 Q_0^3}{E'^2} \right)^{1/9} t_*^{1/9}, \quad p_m = E' \left( \frac{\mu'}{E'} \right)^{1/3} t_*^{-1/3}. \quad (3.7)$$

We interpret these conditions on the dimensionless quantities as follows. Consistent with elementary elasticity, the condition  $\mathcal{G}_e = 1$  implies that the average aperture divided by the fracture dimension is of the same order as the average net pressure divided by the elastic modulus. Consistent with global volume balance, the condition  $\mathcal{G}_v = 1$  requires that the volume of the fracture, represented by the product of the fracture aperture and the area of the fracture footprint characterized by  $l_m^2$ , must match the volume of fluid injected, which is characterized by the product of the

characteristic injection rate  $Q_0$  and the average injection time. The condition  $\mathcal{G}_m = 1$  on the dimensionless viscosity implies that the average pressure matches the viscous pressure drop due to flow between the injection point and the fracture perimeter. With these scalings the remaining dimensionless parameter associated with the fracture toughness  $\mathcal{G}_k$ , which we choose to represent by the symbol  $\mathcal{K}(t_*)$ , assumes the form:

$$\mathcal{G}_k = \mathcal{K}(t_*) = \left( \frac{K'^{18} t_*^2}{E'^{13} \mu'^5 Q_0^3} \right)^{1/18}. \tag{3.8}$$

3.1.2. Toughness dominated propagation

The scaling for the toughness propagation regime can be obtained by requiring that  $\mathcal{G}_e = \mathcal{G}_v = \mathcal{G}_k = 1$ , from which we obtain the following power law relationships between the toughness length scale  $l_k$ , the width scale  $w_k$ , and the pressure scale  $p_k$  as functions of the characteristic time  $t_*$ :

$$l_k = \left( \frac{E' Q_0}{K'} \right)^{2/5} t_*^{2/5}, \quad w_k = \left( \frac{K'^4 Q_0}{E'^4} \right)^{1/5} t_*^{1/5}, \quad p_k = E' \left( \frac{K'^6}{E'^6 Q_0} \right)^{1/5} t_*^{-1/5}. \tag{3.9}$$

With these scalings the dimensionless viscosity  $\mathcal{G}_m$ , which we choose to represent by the symbol  $\mathcal{M}(t_*)$ , assumes the form:

$$\mathcal{G}_m = \mathcal{M}(t_*) = \left( \frac{E'^{13} \mu'^5 Q_0^3}{K'^{18} t_*^2} \right)^{1/5} = \mathcal{K}^{-18/5}. \tag{3.10}$$

3.1.3. Viscous to toughness transition for a radial fracture and intermediate viscosity–toughness scaling

For a radial fracture  $\mathcal{K}$  and  $\mathcal{M}$  depend on time and, as a result, the propagation regime evolves with time. Indeed, from (3.8) we observe that very early in the evolution of a radial fracture the dimensionless toughness  $\mathcal{K}$  is very small so that the majority of the energy required for the fracture to grow is expended in viscous dissipation. Since  $\mathcal{K}$  grows at a rate  $t_*^{1/9}$ , for large times  $\mathcal{K}$  increases till the dominant energy involved in extending the fracture is expended in breaking the rock. Consistent with this evolution in propagation regimes, from (3.10) we observe that the dimensionless viscosity  $\mathcal{M}$  is initially very large and ultimately tends to zero at large times. For a radial fracture the transition time  $t_{mk}$  between these two modes of propagation is determined by the time at which  $\mathcal{K} = 1$ , which is given by

$$t_{mk} = \left( \frac{E'^{13} \mu'^5 Q_0^3}{K'^{18}} \right)^{1/2}. \tag{3.11}$$

The corresponding length, width, and pressure scales are given by

$$l_{mk} = \frac{E'^3 \mu' Q_0}{K'^4}, \quad w_{mk} = \left( \frac{E' \mu' Q_0}{K'^2} \right)^{1/2}, \quad p_{mk} = \left( \frac{K'^6}{E'^3 \mu' Q_0} \right)^{1/2} \tag{3.12}$$

while the characteristic velocity is given by

$$\mathcal{V}_{mk} = \frac{l_{mk}}{t_{mk}} = \left( \frac{K'^{10}}{E'^7 \mu'^3 Q_0} \right)^{1/2}. \tag{3.13}$$

To understand the implications of this, assuming parameter values that might be encountered in the field, we consider a rock with a plane strain modulus  $E' = 60$  GPa; a toughness of  $K_{Ic} = 1$  MPa m<sup>1/2</sup>; and injection of a gel with a viscosity of 0.05 Pa s at a rate of  $Q_0 = 2.65 \times 10^{-2}$  m<sup>3</sup>/s (or 10 barrels per minute). In this case the viscous to toughness transition time  $t_{mk}$  is close to 12.7 years, which is far in excess of the approximately 2 h typical of hydraulic fracture stimulations. On the other hand if, instead of the gel, water having a viscosity of 10<sup>-3</sup> Pa s is injected, then the viscous to toughness transition  $t_{mk}$  occurs within 0.26 s. Recall that these estimates are made assuming a radial fracture, which is implicit in the scaling due to the fact that the  $x$  and  $y$  coordinates were assigned the same length

scale  $l_*$  in (3.1). However, radially symmetric propagation is frequently disturbed by inhomogeneities in the material properties of the host rock often due to sedimentary layering or jumps in the geological confining stress across layer interfaces. In such situations, the mode of propagation is not uniform throughout the fracture, but can vary all along the perimeter of the fracture depending upon the length scale implied by the local velocity of the front. Below we provide numerical examples of this situation in which the fracture footprint is deformed by a pair of stress barriers.

3.2. Tip behavior

3.2.1. Tip equations and the semi-infinite fracture moving with a constant velocity

Provided the fracture front is sufficiently smooth that a finite radius of curvature can be defined at each point along its perimeter, then it can be shown [11] that the governing Eqs. (2.2), (2.5) and (2.6) for the aperture  $w(s, t)$  and net pressure  $p(s)$  in the vicinity of the fracture front reduce to those for a semi-infinite fluid-driven fracture steadily propagating at a constant velocity  $V$  and characterized by zero lag (see [20,29]), namely:

$$\frac{\hat{w}^3}{\mu'} \frac{d\hat{p}}{ds} = V \hat{w}, \quad \hat{p} = \frac{E'}{4\pi} \int_0^\infty \frac{d\hat{w}}{dz} \frac{dz}{s-z}, \quad \lim_{s \rightarrow 0} \frac{\hat{w}}{s^{1/2}} = \frac{K'}{E'}. \tag{3.14}$$

Here  $s$  represents a coordinate located on the moving tip and pointing toward the interior of the fracture. The consequence of this reduction is profound in that the tip asymptotic solution for a *finite fracture* at any time is given by the solution of the stationary semi-infinite crack problem whose constant tip velocity corresponds to the *current* propagation speed of the finite fracture. The tip solution is thus autonomous. Note that the spatial variation of the far-field stress can be ignored when viewed at the tip scale, unless the stress field is discontinuous (in which case, the tip solution outlined here is not relevant).

3.2.2. Scaling the semi infinite fracture equations

We introduce the characteristic tip length scale  $\hat{L}_*$ , the characteristic tip opening  $\hat{W}_*$ , and the characteristic pressure  $\hat{P}_*$  as well as the normalized distance from the tip  $\hat{\xi}$ . The tip opening and net pressure asymptotics can now be expressed as  $\hat{\Omega}(\hat{\xi})$  and  $\hat{\Pi}(\hat{\xi})$ , where

$$s = \hat{L}_* \hat{\xi}, \quad \hat{w} = \hat{W}_* \hat{\Omega}, \quad \hat{p} = \hat{P}_* \hat{\Pi}. \tag{3.15}$$

With these scalings the governing Eq. (3.14) become

$$\frac{1}{\hat{G}_m} \hat{\Omega}^2 \frac{d\hat{\Pi}}{d\hat{\xi}} = 1, \quad \hat{\Pi} = \frac{\hat{G}_e}{4\pi} \int_0^\infty \frac{d\hat{\Omega}}{d\hat{\xi}'} \frac{d\hat{\xi}'}{\hat{\xi} - \hat{\xi}'}, \quad \lim_{\hat{\xi} \rightarrow 0} \frac{\hat{\Omega}}{\hat{\xi}^{1/2}} = \hat{G}_k \tag{3.16}$$

where

$$\hat{G}_e = \frac{E' \hat{W}_*}{\hat{P}_* \hat{L}_*}, \quad \hat{G}_m = \frac{\mu' \hat{L}_* V}{W_*^2 \hat{P}_*}, \quad \hat{G}_k = \frac{K' \hat{L}_*^{1/2}}{E' \hat{W}_*}. \tag{3.17}$$

*Viscous regime:*

We impose the condition  $\hat{G}_e = \hat{G}_m = 1$ , from which we obtain the following fundamental power law relations:

$$\hat{W}_* = \hat{L}_m^{1/3} \hat{L}_*^{2/3} \quad \text{and} \quad \hat{P}_* = E' \left( \frac{\hat{L}_m}{\hat{L}_*} \right)^{1/3}. \tag{3.18}$$

Here  $\hat{L}_m = \frac{\mu' V}{E'}$  is the viscous length scale, and if we choose  $\hat{L}_* = \hat{L}_m$  then  $\hat{W}_* = \hat{L}_m$ , and  $\hat{P}_* = E'$ .

*Toughness regime:*

We impose the condition  $\hat{G}_e = \hat{G}_k = 1$ , from which we obtain the following fundamental power law relations:

$$\hat{W}_* = \hat{L}_k^{1/2} \hat{L}_*^{1/2} \quad \text{and} \quad \hat{P}_* = E' \left( \frac{\hat{L}_k}{\hat{L}_*} \right)^{1/2}. \tag{3.19}$$

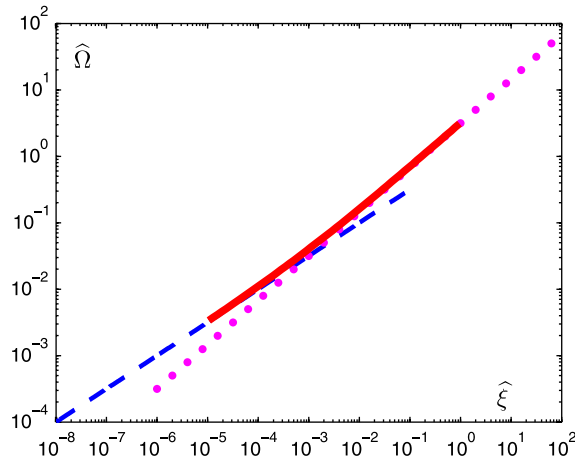


Fig. 2. The stationary solution  $\hat{\Omega}(\hat{\xi})$  for a semi-infinite fracture propagating with a constant velocity  $V$  is denoted by the solid line (colored red online). The toughness asymptote, represented by the dashed line (colored blue online), is valid for  $\hat{\xi} \lesssim \hat{\xi}_k = 10^{-5}$ . The viscous asymptote, represented by the dotted line (colored magenta online), is valid for  $\hat{\xi} \gtrsim \hat{\xi}_m = 10^{-1}$ .

Here  $\hat{L}_k = \left(\frac{K'}{E'}\right)^2$  is the toughness length scale, and if we choose  $\hat{L}_* = \hat{L}_k$  then  $\hat{W}_* = \hat{L}_k$ , and  $\hat{P}_* = E'$ .

*Intermediate/viscosity–toughness scaling:*

If we wish to identify the length scale  $\hat{L}_*$  at which both the fundamental width asymptotes (3.18) and (3.19) are both valid then

$$\hat{W}_* = \hat{L}_m^{1/3} \hat{L}_*^{2/3} = \hat{L}_k^{1/2} \hat{L}_*^{1/2}. \tag{3.20}$$

Using this condition, we obtain the intermediate length scale  $\hat{L}_{mk}$  and the characteristic opening  $\hat{W}_{mk}$  and pressure  $\hat{P}_{mk}$ , which can be expressed as follows:

$$\hat{L}_{mk} = \frac{\hat{L}_k^3}{\hat{L}_m^2} = \frac{K'^6}{E'^4 \mu'^2 V^2}, \quad \hat{W}_{mk} = \frac{\hat{L}_k^2}{\hat{L}_m} = \frac{K'^4}{E'^3 \mu' V}, \quad \hat{P}_{mk} = E' \frac{\hat{L}_m}{\hat{L}_k} = \frac{E'^2 \mu' V}{K'^2}. \tag{3.21}$$

In the intermediate scalings (3.21), for which  $\hat{\mathcal{G}}_e = \hat{\mathcal{G}}_m = \hat{\mathcal{G}}_k = 1$ , a detailed asymptotic analysis [13,20,29] of the governing Eqs. (3.16) yields the following asymptotic expansions for  $\hat{\Omega}(\hat{\xi})$

$$\hat{\xi} \rightarrow 0: \quad \hat{\Omega} = \hat{\xi}^{1/2} + 4\pi \hat{\xi} + \frac{128}{3} \hat{\xi}^{3/2} \ln \hat{\xi} + O(\hat{\xi}^{3/2}) \tag{3.22}$$

$$\hat{\xi} \rightarrow \infty: \quad \hat{\Omega} = \beta_0 \hat{\xi}^{2/3} + \beta_1 \hat{\xi}^h + o(\hat{\xi}^h) \tag{3.23}$$

where  $\beta_0 = 2^{1/3} \cdot 3^{5/6}$ ,  $\beta_1 \simeq 0.0371887$ , and  $h \simeq 0.138673$ . The complete semi-infinite tip solution to (3.16), which was obtained by numerical solution in [13], is plotted in Fig. 2, where it can be seen that the LEFM behavior ( $\hat{\xi}^{1/2}$ ) applies for  $\hat{\xi} \lesssim \hat{\xi}_k = 10^{-5}$  and the viscous dissipation asymptote ( $\hat{\xi}^{2/3}$ ) applies for  $\hat{\xi} \gtrsim \hat{\xi}_m = 10^{-1}$ .

*Mapping the tip of a planar fracture to a semi-infinite fracture moving at a constant speed V:*

We relate the finite and semi infinite scalings as follows

$$s = \hat{L}_{mk} \hat{\xi} = l_{mk} \xi \quad \text{and} \quad \hat{w}(s) = \hat{W}_{mk} \hat{\Omega}(\hat{\xi}) = w_{mk} \Omega(\xi). \tag{3.24}$$

Introducing the dimensionless velocity  $v$ , we relate the semi-infinite fracture velocity  $V$  to the characteristic finite fracture velocity  $\mathcal{V}_{mk}$ , defined in (3.13), as follows:

$$V = \mathcal{V}_{mk} v. \tag{3.25}$$

The semi infinite and finite scaled coordinates and widths can be expressed succinctly in terms of the dimensionless velocity  $v$  as follows:

$$\frac{l_{mk}}{\hat{L}_{mk}} = v^2 \quad \text{and} \quad \frac{w_{mk}}{\hat{W}_{mk}} = v \tag{3.26}$$

from which it follows that

$$\hat{\xi} = v^2 \xi \quad \text{and} \quad \hat{\Omega} = v \Omega. \tag{3.27}$$

The fundamental mapping between the scaled width function  $\Omega(\xi)$  and the universal asymptote  $\hat{\Omega}(\hat{\xi})$  is thus given by

$$\Omega(\xi) = \frac{1}{v} \hat{\Omega}(v^2 \xi). \tag{3.28}$$

#### 4. Implementing the generalized asymptote within the implicit level set algorithm (ILSA)

##### 4.1. Discrete equations

We assume [11] that the fracture will grow within a rectangular region that has been tessellated into a fixed uniform rectangular mesh  $\cup \Delta \mathcal{A}_{m,n}$  with dimensions  $\Delta \chi$  and  $\Delta \zeta$  in the two coordinate directions (similar to the unscaled fracture shown in Fig. 1). The fracture footprint  $\mathcal{A}(\tau)$  is then covered by rectangular elements  $\Delta \mathcal{A}_{m,n}$  such that  $\mathcal{A} \subseteq \cup \Delta \mathcal{A}_{m,n}$ . Constant displacement discontinuity (DD) elements are used for the elasticity computations [26] along with collocation at element centers, while the lubrication equation is discretized via the finite volume method to yield a five node finite difference stencil [25]. The resulting, extremely stiff, system of ODEs is solved using the backward Euler scheme. Finally, assuming that the front positions in each of the tip elements is known from the Level Set scheme described below, the tip asymptote (3.28) is used to set the fracture aperture in each tip element to be equal to the average fluid volume contained within that particular element. This approach makes it possible to impose the tip asymptotic behavior on the solution in a weak sense. Since the tip elements are treated differently, it is notionally convenient to separate the DD elements representing the fracture into two sets, namely: the tip elements  $\mathcal{A}^t$  and the channel elements  $\mathcal{A}^c$ . The tip elements are the partially filled elements colored by light shading in Fig. 1, while the channel elements comprise those elements surrounded by the tip elements that are completely filled with fluid.

##### 4.1.1. Discrete elasticity equation

The elasticity equation (3.3) is discretized by assuming that the fracture opening  $\Omega(\chi, \zeta, \tau)$  is piecewise constant over each rectangular element  $\mathcal{A}_{m,n}$ , i.e.

$$\Omega(\chi, \zeta, \tau) = \sum_{m,n} \Omega_{m,n}(\tau) H_{m,n}(\chi, \zeta) \tag{4.1}$$

in which

$$H_{m,n}(\chi, \zeta) = \begin{cases} 1 & \text{for } (\chi, \zeta) \in \mathcal{A}_{m,n} \\ 0 & \text{for } (\chi, \zeta) \notin \mathcal{A}_{m,n} \end{cases} \tag{4.2}$$

is the characteristic function for element  $(m, n)$ . Substituting this expansion into the integral equation (3.3) and evaluating the pressures at the collocation points located at the element centers, yields a system of algebraic equations of the form

$$\Pi_{k,l}(\tau) = \sum_{m,n} C_{k-m,l-n} \Omega_{m,n}(\tau) \tag{4.3}$$

where

$$C_{k-m,l-n} = -\frac{1}{8\pi} \left[ \frac{\sqrt{(\chi_k - \chi)^2 + (\zeta_l - \zeta)^2}}{(\chi_k - \chi)(\zeta_l - \zeta)} \right]_{\chi=\chi_m - \Delta\chi/2, \zeta=\zeta_n - \Delta\zeta/2}^{\chi=\chi_m + \Delta\chi/2, \zeta=\zeta_n + \Delta\zeta/2}.$$

It is also convenient to express the discretized elasticity equation (4.3) in the following operator form

$$\mathbf{\Pi} = \mathbf{C}\mathbf{\Omega}. \tag{4.4}$$

4.1.2. Discrete Reynolds equation

Integrating the Reynolds equation (3.4) over the time interval  $[\tau - \Delta\tau, \tau]$  and over the element  $\mathcal{A}_{k,l}$  and applying the divergence theorem we obtain

$$\int_{\mathcal{A}_{k,l}} \Omega(\tau) - \Omega(\tau - \Delta\tau) dA = \Delta\tau \left[ \int_{C_{k,l}} \Omega^3 \frac{\partial \Pi}{\partial n} dC \right]_{\tau} + \Delta_{k0,l0} \int_{\tau - \Delta\tau}^{\tau} \psi(\tau') d\tau' \tag{4.5}$$

where  $\Delta_{k0,l0}$  is the Kronecker delta symbol and  $C_{k,l}$  represents the boundary of the  $(k, l)$ th element. In order to discretize the integral form of the fluid flow equation (4.5) in a way that is compatible with (4.3) we use the pressures  $\Pi_{k,l}(\tau)$  and average widths  $\Omega_{k,l}(\tau)$  sampled at element centers along with central difference approximations to the pressure gradients on the boundaries of the elements, and divide by  $\Delta\chi \Delta\zeta$  to obtain

$$\Omega_{k,l}(\tau) - \Omega_{k,l}(\tau - \Delta\tau) = \Delta\tau [A(\Omega)\Pi]_{k,l} + \frac{\Delta_{k0,l0}}{\Delta\chi \Delta\zeta} \int_{\tau - \Delta\tau}^{\tau} \psi(\tau') d\tau' \tag{4.6}$$

where  $A(\Omega)$  is the difference operator defined by

$$[A(\Omega)\Pi]_{k,l} = \frac{\Psi_{k+\frac{1}{2},l} - \Psi_{k-\frac{1}{2},l}}{\Delta\chi} + \frac{\Psi_{k,l+\frac{1}{2}} - \Psi_{k,l-\frac{1}{2}}}{\Delta\zeta}. \tag{4.7}$$

Here  $\Psi_{k\pm\frac{1}{2},l}$  are the fluxes along the vertical edges of the element defined as  $\Psi_{k\pm\frac{1}{2},l} = \pm \Omega_{k\pm\frac{1}{2},l}^3 \left( \frac{\Pi_{k\pm 1,l} - \Pi_{k,l}}{\Delta\chi} \right)$ , where  $\Omega_{k\pm\frac{1}{2},l}$  are the corresponding edge widths defined by  $\Omega_{k\pm\frac{1}{2},l} = \left( \frac{\Omega_{k\pm 1,l} + \Omega_{k,l}}{2} \right)$ . The fluxes and widths along the horizontal edges of the element are defined analogously. Zero flux boundary conditions are implemented in tip elements by removing those terms associated with the element faces having zero boundary fluxes from the difference operator.

The discrete lubrication equation (4.6) can be expressed in the following operator form

$$\Delta\mathbf{\Omega} = \Delta\tau \mathbf{A}(\mathbf{\Omega})\mathbf{\Pi} + \mathbf{F} \tag{4.8}$$

where  $\mathbf{A}(\mathbf{\Omega})$  is the second order difference operator defined on the right side of (4.7) and  $\mathbf{F}$  represents the vector of source terms.

4.1.3. The coupled width–pressure equations

Once the front position in a tip element has been defined, the width profile within the element is determined by the applicable tip asymptotic solution as given above and the corresponding tip fluid volume can be calculated by direct integration (see Section 4.2.3). Thus the fracture width in the tip elements can no longer be used as a primary variable. To conserve fluid volume, average width values calculated from the tip fluid volumes must then be allocated to the DD element tip width values in a way that is consistent with the volume of fluid that has flowed into the tip element. Thus the primary unknowns within the tip elements become the fluid pressures, which are calculated in such a way that mass balance is preserved. We now provide details of the computation of the mixed field variables.

Since we treat the tip and channel variables differently, we introduce a superscript  $c$  to represent a channel variable and a superscript  $t$  to represent a tip variable. Thus  $\mathbf{\Omega}^c$  and  $\mathbf{\Pi}^c$  represent the vectors containing the channel widths and fluid pressures respectively, while  $\mathbf{\Omega}^t$  and  $\mathbf{\Pi}^t$  represent the corresponding tip variables. From (4.4) the channel pressures can be expressed as

$$\mathbf{\Pi}^c = \mathbf{C}^{cc} \mathbf{\Omega}^c + \mathbf{C}^{ct} \mathbf{\Omega}^t \tag{4.9}$$

where  $\mathbf{C}^{cc}$  and  $\mathbf{C}^{ct}$  represent the channel-to-channel and tip-to-channel Green’s function influence matrices. From (4.8) the channel lubrication equation can be written in the form

$$\Delta\mathbf{\Omega}^c = \mathbf{\Omega}^c - \mathbf{\Omega}_0^c = \Delta\tau (\mathbf{A}^{cc} \mathbf{\Pi}^c + \mathbf{A}^{ct} \mathbf{\Pi}^t) + \Delta\tau \mathbf{F}^c \tag{4.10}$$

where  $\Omega_0^c$  is the channel width at the previous time step. For the tip, the lubrication equation (4.8) can be re-written as

$$\Delta\Omega^t = \Omega^t - \Omega_0^t = \Delta\tau (A^{tc} \mathbf{II}^c + A^{tt} \mathbf{II}^t) + \Delta\tau \mathbf{I}^t. \quad (4.11)$$

Now using (4.9) to eliminate  $\mathbf{II}^c$  from (4.10) and (4.11) and re-arranging terms, we obtain the following system of non-linear equations for the channel width increments and tip pressures:

$$\begin{bmatrix} \mathbf{I} - \Delta\tau \mathbf{A}^{cc} \mathbf{C}^{cc} & -\Delta\tau \mathbf{A}^{ct} \\ -\Delta\tau \mathbf{A}^{tc} \mathbf{C}^{cc} & -\Delta\tau \mathbf{A}^{tt} \end{bmatrix} \begin{bmatrix} \Delta\Omega^c \\ \mathbf{II}^t \end{bmatrix} = \begin{bmatrix} \Delta\tau \mathbf{A}^{cc} (\mathbf{C}^{cc} \Omega_0^c + \mathbf{C}^{ct} \Omega^t) + \Delta\tau \mathbf{I}^c \\ -\Delta\Omega^t + \Delta\tau \mathbf{A}^{tc} (\mathbf{C}^{cc} \Omega_0^c + \mathbf{C}^{ct} \Omega^t) + \Delta\tau \mathbf{I}^t \end{bmatrix}. \quad (4.12)$$

Since the front positions and therefore the tip widths  $\Omega^t$  are assumed to be known, the solution to this system of equations yields the channel widths  $\Omega^c = \Omega_0^c + \Delta\Omega^c$  and the tip pressures  $\mathbf{II}^t$ . By freezing the matrix coefficients and the right hand side components at the current trial solution, we obtain a linear system for  $\Delta\Omega^c$  and  $\mathbf{II}^t$ . Efficient preconditioners for this system of linear equation (4.12) can be found in [31,32]. The value of  $\Delta\Omega^c$  is then used to update the trial solution  $\Omega^c$  and the process is repeated to yield a fixed-point iteration scheme that is continued until convergence is achieved.

## 4.2. The implicit level set algorithm ILSA-MK

### 4.2.1. Determining the distance to the free boundary by inverting the generalized asymptote

Having determined the trial fracture widths  $\Omega^c$  in the channel elements and tip pressures  $\mathbf{II}^t$  by solving the coupled pressure–width equation (4.12), the trial solution for the channel widths along with the stationary solution  $\widehat{\Omega}(\widehat{\xi})$  can be used to determine a new estimate for the location of the free boundary  $\mathcal{C}(\tau)$ . In the ribbon of channel elements  $\partial\mathcal{A}^c$  on the boundary of the channel region  $\mathcal{A}^c$  that share at least one side with a tip element (see the dark shaded elements in Fig. 1), the current trial fracture widths are used to determine the shortest distance  $\xi$  from the centers of these elements to the free boundary. At each of these collocation points, the fundamental mapping between the known fracture width  $\Omega(\xi)$  and the corresponding abscissa in the universal asymptote shown in Fig. 2 is given by (3.28). In this equation the dimensionless velocity  $v$  in the direction normal to the front is also unknown. However, assuming that the distance  $\xi_0$  to the previous front is known and that  $\xi$  is the distance to the current front that we desire, an approximation to this normal velocity can be expressed as

$$v = \frac{\xi - \xi_0}{\Delta\tau}. \quad (4.13)$$

Using (4.13) to eliminate the normal velocity  $v$  from (3.28), we obtain the following nonlinear equation from which we can obtain the shortest distance  $\xi$  to the free boundary corresponding to a given  $\Omega$ :

$$\Omega - \frac{\Delta\tau}{\xi - \xi_0} \widehat{\Omega} \left( \left( \frac{\xi - \xi_0}{\Delta\tau} \right)^2 \xi \right) = 0. \quad (4.14)$$

The monotonic function  $\widehat{\Omega}(\widehat{\xi})$  is approximated as follows: on the interval  $[0, 10^{-5}]$  we use the toughness asymptote (3.22); within the intermediate interval  $[10^{-5}, 10^0]$ , on which the values of  $\widehat{\Omega}$  are represented in Fig. 2 by a solid red line, we interpolate the numerical values of  $\widehat{\Omega}$  in log–log space by a spline function; and on  $[10^0, \infty)$  we use the viscous asymptote (3.23).

### 4.2.2. Locating the free boundary by solving the eikonal equation

Having determined the shortest distance from the collocation points to the free boundary for each element of the ribbon of channel elements adjacent to the tip elements, these distances are used as initial conditions

$$\mathcal{T}^0(\chi, \zeta) = -\xi \quad \text{for all } (\chi, \zeta) \in \partial\mathcal{A}^c \quad (4.15)$$

to construct the signed distance function  $\mathcal{T}(\chi, \zeta)$  by solving the eikonal equation

$$|\nabla\mathcal{T}| = 1. \quad (4.16)$$

The negative sign in the initial condition (4.15) enforces the sign convention that  $\mathcal{T}(\chi, \zeta) < 0$  for all points  $(\chi, \zeta)$  that lie within the fracture boundary curve  $\mathcal{C}(\tau)$ , while points for which  $\mathcal{T}(\chi, \zeta) > 0$  lie outside  $\mathcal{C}(\tau)$ . Moreover, because

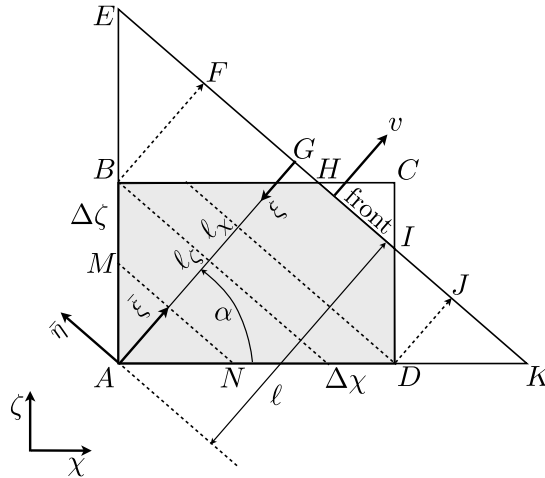


Fig. 3. Scheme to integrate the universal asymptotic solution, backwards from the front, over the partially filled rectangular tip element ABCD.

the initial condition (4.15) defines the distance to the free boundary, the fracture boundary curve  $\mathcal{C}(\tau)$  is defined by the level set  $\mathcal{T}(\chi, \zeta) = 0$ .

Using a simple first order scheme [33,34] to discretize the Hamilton–Jacobi equation (4.16), it is possible [11] to use two neighboring values  $\mathcal{T}_{m-1,n}$  and  $\mathcal{T}_{m,n-1}$  to determine  $\mathcal{T}_{m,n}$  using the formula

$$\mathcal{T}_{m,n} = \frac{\mathcal{T}_{m-1,n} + \beta \mathcal{T}_{m,n-1} + \Theta}{1 + \beta^2} \tag{4.17}$$

where  $\Theta = \sqrt{\Delta\chi^2(1 + \beta^2) - \beta^2 \Delta\mathcal{T}^2}$ ,  $\beta = \Delta\chi/\Delta\zeta$ , and  $\Delta\mathcal{T} = \mathcal{T}_{m,n-1} - \mathcal{T}_{m-1,n}$ . The fast marching method [33] is then used to extend the initial values of  $\mathcal{T}_{m,n}^0$  of the signed distance function along  $\partial\mathcal{A}^c$  to a narrow band that includes the fracture front. Using this solution, the location of the fracture front in a tip element is defined by

$$\ell = -\left(\frac{\mathcal{T}_{m,n-1} + \mathcal{T}_{m-1,n}}{2}\right) \quad \text{and} \quad \tan \alpha = \frac{\beta(\Theta - \Delta\mathcal{T})}{\Theta + \beta^2 \Delta\mathcal{T}} \tag{4.18}$$

where  $\ell$  is the distance from the front to the farthest interior corner of a tip element (line segment  $\overline{AG}$  in Fig. 3) and  $\alpha$  is the angle that the local outward normal to the front makes with the tip element edge as shown in Fig. 3. Finally, the normal velocity field can be determined using

$$v = \frac{\mathcal{T}(\chi, \zeta, \tau - \Delta\tau) - \mathcal{T}(\chi, \zeta, \tau)}{\Delta\tau}. \tag{4.19}$$

### 4.2.3. Tip volume calculation

Since the DD method assigns the width field in a partially filled tip element to be the average volume of fluid contained in that element, it is necessary to determine this fluid volume. Once the level set scheme has been used to determine the current location  $\ell$ , orientation  $\alpha$ , and normal speed of the front  $v$ , the fluid volume corresponding to the tip asymptote can be calculated. The procedure used to determine this tip volume is depicted in Fig. 3. In this figure the fluid is shown to fill the polygonal region  $ABHID$  within the rectangular element  $ABCD$  of size  $\Delta\chi \times \Delta\zeta$  in which the fracture front  $HI$  is a distance  $\ell$  from the bottom left vertex of the element (point A) and moving at a speed  $v$  in a direction with direction cosines  $(\cos \alpha, \sin \alpha)$ . The line parallel to the front and passing through B is a distance  $\ell_\zeta = \Delta\zeta \sin \alpha$  from the point A, while that parallel to the front and passing through D is a distance  $\ell_\chi = \Delta\chi \cos \alpha$  from A. The maximum value  $\Lambda$  that  $\ell$  achieves, when the front passes through the point C, is given by

$$\Lambda = \overrightarrow{AC} \cdot (\cos \alpha, \sin \alpha) = \Delta\chi \cos \alpha + \Delta\zeta \sin \alpha = \ell_\chi + \ell_\zeta. \tag{4.20}$$

When the front is moving horizontally,  $\alpha = 0$  so that  $\ell_\chi = \Delta\chi$  and  $\ell_\zeta = 0$ , while for a front that is moving vertically,  $\alpha = \pi/2$  so that  $\ell_\chi = 0$  and  $\ell_\zeta = \Delta\zeta$ .

Now observing that the length of  $\overline{MN}$  can be expressed in the form

$$|\overline{MN}| = \frac{\bar{\xi}}{\cos \alpha \sin \alpha} = m\bar{\xi}, \quad \text{where } m = \frac{1}{\cos \alpha \sin \alpha}, \tag{4.21}$$

the volume of the fracture in the triangular region  $AEK$  is given by

$$\mathcal{V}(\ell) = \int_0^\ell \Omega(\ell - \bar{\xi})m\bar{\xi}d\bar{\xi}. \tag{4.22}$$

Making the transformation  $\hat{\xi} = (\ell - \bar{\xi})v^2 = \xi v^2$  and using the mapping formula (3.28), we obtain the following expression for  $\mathcal{V}(\ell)$  in terms of the universal asymptote  $\widehat{\Omega}(\hat{\xi})$ ;

$$\mathcal{V}(\ell) = \frac{m}{v^5} \left\{ \ell v^2 \mathcal{V}_0(\ell) - \mathcal{V}_1(\ell) \right\} \tag{4.23}$$

where  $\mathcal{V}_0(\ell) = \int_0^{\ell v^2} \widehat{\Omega}(\hat{\xi})d\hat{\xi}$  and  $\mathcal{V}_1(\ell) = \int_0^{\ell v^2} \widehat{\Omega}(\hat{\xi})\hat{\xi}d\hat{\xi}$  are the zeroth and first moments of  $\widehat{\Omega}$ . In the definition of  $\mathcal{V}(\ell)$  no reference is made to the rectangle  $ABCD$ . Indeed,  $\mathcal{V}(\ell)$  may be defined to be the volume associated with the universal asymptote that is trapped in the triangular region that is completely determined by the normal distance  $\ell$  from the front moving with a speed  $v$  and whose direction of propagation is defined by  $\alpha$ . Thus the dimensions of the rectangular element  $ABCD$  do not enter the expression for  $\mathcal{V}(\ell)$ . The formula for  $\mathcal{V}$  can therefore be used to define the volume associated with the universal asymptote that is trapped within any triangle that is similar to  $AEK$ . Two such triangles of particular importance are  $BEH$  and  $DIK$ . Since  $|\overline{BF}| = \ell - \ell_\zeta$  and  $|\overline{DJ}| = \ell - \ell_\chi$ , it follows that the volume within the triangular region  $BEH$  is given by  $\mathcal{V}(\ell - \ell_\zeta)$ , while that within the triangular region  $DIK$  is given by  $\mathcal{V}(\ell - \ell_\chi)$ . Using these triangular volumes it follows that the volume of the tip asymptote in the pentagonal region  $ABHID$  is given by

$$\mathcal{V}_{ABHID} = \mathcal{V}(\ell) - \mathcal{V}(\ell - \ell_\zeta) - \mathcal{V}(\ell - \ell_\chi). \tag{4.24}$$

In Fig. 3 and in the subsequent analysis  $\ell_\chi > \ell_\zeta$ , whereas the case  $\ell_\chi < \ell_\zeta$  can be treated analogously. To represent both cases it is convenient to define

$$\ell_0 = \min \{ \ell_\chi, \ell_\zeta \} \quad \text{so that } \Lambda - \ell_0 = \max \{ \ell_\chi, \ell_\zeta \}. \tag{4.25}$$

Similar to (4.24), it is possible to use the volume for a triangular region (4.23) as a basic building-block to construct the volume  $\mathcal{V}_{i,j}(\ell)$  associated with the tip asymptote over the  $i, j$ th tip element having any possible configuration. Indeed, the elemental tip volumes  $\mathcal{V}_{i,j}(\ell)$  for all the different cases in which the fluid-filled region can be a triangle, a quadrilateral, or a pentagon, are summarized as follows:

$$\mathcal{V}_{i,j}(\ell) = \begin{cases} \mathcal{V}(\ell) - H(\ell - \ell_0)\mathcal{V}(\ell - \ell_0) - H(\ell + \ell_0 - \Lambda)\mathcal{V}(\ell + \ell_0 - \Lambda), & 0 \leq \ell \leq \Lambda, m \neq \infty \\ \Delta\zeta \mathcal{V}_0(\ell)/v^3, & 0 \leq \ell \leq \Delta\xi, \alpha = 0 \\ \Delta\xi \mathcal{V}_0(\ell)/v^3 & 0 \leq \ell \leq \Delta\zeta, \alpha = \pi/2 \end{cases} \tag{4.26}$$

where  $H(s)$  is the Heaviside Step function. Finally, the average fracture aperture  $\Omega_{i,j}$  is defined in terms of the asymptotic tip volume as follows:

$$\Omega_{i,j} = \frac{\mathcal{V}_{i,j}(\ell)}{\Delta\chi \Delta\zeta}. \tag{4.27}$$

The fact that the average tip apertures encapsulate, in a weak sense, all the multi-scale tip asymptotic behavior right down to the finest scale has profound consequences in terms of modeling efficiency. Typically for radial fractures the tip asymptote is valid within a distance that is 10% of the radius from the crack tip, i.e.  $0.1\gamma$ . Now consider modeling a hydraulic fracture that is propagating in the viscous regime in which the effects of toughness are sub-dominant, but not negligible. Capturing the finest length scale active in this problem directly would require that we choose the smallest element size to match the finest length scale. Modeling such multi-scale behavior directly would require prohibitively fine meshes (see [12]). However, since the tip averaging process just described accounts for this multi-scale behavior albeit in an average sense, we are able capture the effect of this finer-scale behavior even though we only set the mesh

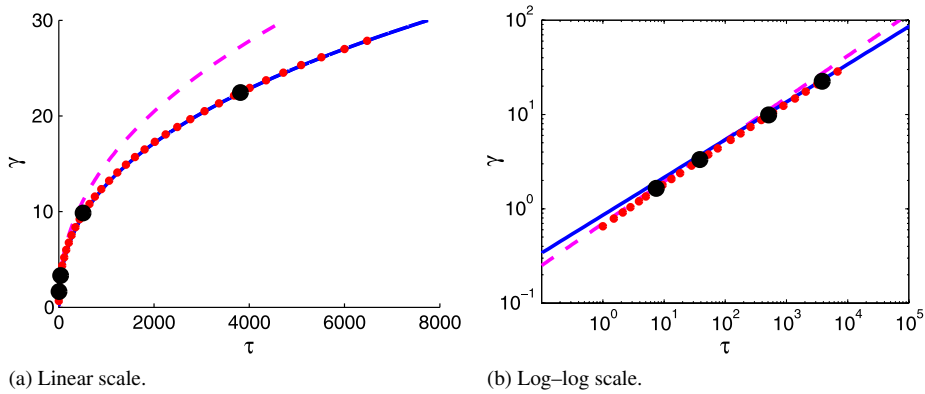


Fig. 4. Left: Evolution of the fracture radius  $\gamma$  plotted on a linear scale. Right: Evolution of the fracture radius  $\gamma$  plotted on a log–log scale. The multi-scale ILSA-MK solution is denoted by the small circles (colored red online), the M-vertex solution is denoted by the dashed line (colored magenta online), and the near K-vertex solution is denoted by the solid line (colored blue online). The large black circles represent the points at which the pressures and widths are sampled in Fig. 5. (For interpretation of the references to color in this figure legend, the reader is referred to the web version of this article.)

size to match the dominant length scale active in the problem. Thus the algorithm is able to represent, in a weak sense, all the fine-scale structure of the problem on a relatively coarse mesh.

### 5. Numerical results

In this section we present numerical results that illustrate the performance of the new ILSA-MK algorithm. For the first test problem, we compare the results obtained using the new algorithm with a reference solution for a propagating radial fracture that traverses the  $\mathcal{M}$ – $\mathcal{K}$  edge of phase space (see [11]). This example illustrates that the implementation of the universal asymptote enables the ILSA-MK scheme to faithfully capture the multi-scale tip behavior on a relatively coarse mesh, whose mesh size is dictated by the desired accuracy for the discretization of the elasticity and lubrication equations and not by the finest length scale active in the problem. In the second test problem, we consider a fracture that propagates in an elastic medium in which there are positive jumps in the confining stress field located symmetrically with respect to the fluid source. This example is chosen to illustrate the way in which the new ILSA scheme is able to capture the different length scales that are active at different points along the perimeter of the fracture, depending upon the magnitude of the local normal velocity.

#### 5.1. $\mathcal{M}$ – $\mathcal{K}$ transition of a radial fracture

As a reference solution for this problem we use the radial solution provided by [14]. The ILSA scheme uses a fixed mesh in which  $\Delta\chi = \Delta\zeta = 0.16$  and initial solution set to the M-vertex radial solution (see [35] or Appendix C.2 in [11]) with a starting radius of  $\gamma = 0.6506$ , which corresponds to a time  $\tau = 0.996$ . In order to be able to cover a large range of times in a single simulation we use the following scheme to adapt the time step

$$\Delta\tau = \frac{1}{2} \min_{(\chi,\zeta) \in \mathcal{A}^t} \frac{A}{v}. \tag{5.1}$$

The ILSA solution was determined for  $\tau \in [0.996, 6.8608 \times 10^3]$  during which  $\mathcal{K} = \tau^{1/9} \in [0.9996, 2.6685]$ .

In Fig. 4 we plot the evolution of the fracture radius  $\gamma$  on (a) linear and (b) log–log scales to emphasize the transition from the M-vertex solution to the near K-vertex solution (see [11]). We observe that the multi-scale ILSA scheme is able to faithfully capture the intermediate solution from close to the M-vertex solution all the way to the near K-vertex solution.

In Fig. 5 we plot the spatial distribution of (a) the fracture opening  $\Omega$  and (b) the fluid pressure  $\Pi$  versus the normalized fracture radius  $\rho$  for a selection of values of the dimensionless toughness  $\mathcal{K}$ . The multi-scale ILSA solution shows close agreement with the reference solution [14] across the range of  $\mathcal{K}$  values considered. The largest discrepancy between these solutions corresponds to  $\mathcal{K} = 1.25$ , which, since it is early in the simulation, corresponds to a relatively coarse mesh. We observe that even though the transition value is nominally  $\mathcal{K} = 1$ , the ILSA and reference solutions

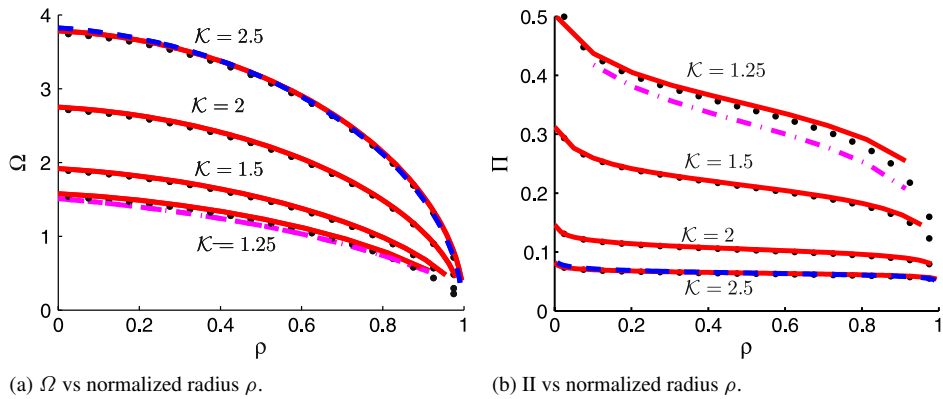


Fig. 5. Left: Fracture opening  $\Omega$  vs normalized fracture radius  $\rho$  for different values of the dimensionless toughness  $\mathcal{K}$ . Right: Fluid pressure  $\Pi$  vs normalized fracture radius  $\rho$  for different values of the dimensionless toughness  $\mathcal{K}$ . The multi-scale ILSA values are denoted by the solid red lines, the reference solution [14] is denoted by the solid black circles, the M-vertex solution is denoted by the dash-dotted magenta lines, and the near K-vertex solution is denoted by the dashed blue lines. The snapshots shown correspond to the large black circles shown in Fig. 4. (For interpretation of the references to color in this figure legend, the reader is referred to the web version of this article.)

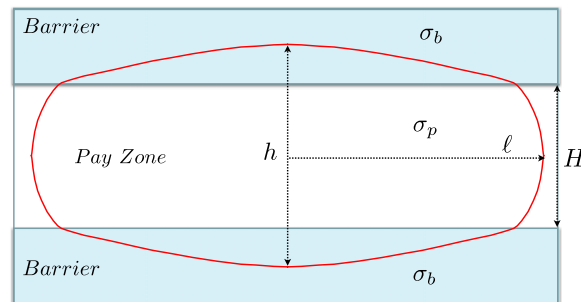


Fig. 6. A blade-shaped fracture formed by a jump in the confining stress field from a value  $\sigma_p$  within a pay zone to a level  $\sigma_b$  within two symmetric stress barriers. The fracture extends beyond the pay-zone of height  $H$  to achieve a maximum height  $h$  while the fracture half-length is denoted by  $\ell$ .

for  $\mathcal{K} = 1.25$  are still fairly close to the M-vertex solution. By the time  $\mathcal{K} = 2.5$ , the ILSA and reference solutions are virtually indistinguishable from the K-vertex solution. It should be noted that the multi-scale ILSA scheme, which in spite of the fact that it uses a structured rectangular mesh, provides an accurate solution to this radially symmetric problem because of the weak form representation of the fracture opening in the partially filled tip elements. This example demonstrates that incorporating the universal asymptote into the ILSA scheme makes it possible to capture the full range of length scales accurately using a relatively coarse mesh. This is achieved by autonomously adjusting the appropriate length scale to the computational mesh, while also capturing the complete fine-scale structure of the tip solution appropriate to the computational mesh scale by imposing the complete tip asymptotics in a weak form.

## 5.2. A symmetric stress barrier: distinct propagation regimes along the periphery

In this section we consider a hydraulic fracture that starts off radially symmetric and which is subsequently deformed into a blade-like geometry when it encounters positive jumps in the confining stress field that are situated symmetrically about the injection point (see Fig. 6). We compare the ILSA results to the stress jump experiment [15] for the viscous case  $K' = 0$  and use the ILSA-MK algorithm to provide results in which the multi-scale effects of viscous dissipation and fracture toughness are included using the universal asymptote. We then use the algorithm to establish the range of applicability of pseudo 3D (P3D) models [18,19,16] that are widely used to design fracture treatments in the oil and gas industry.

### 5.2.1. Comparison with an M-vertex experiment and extension to toughness via ILSA-MK

Since there is no analytic solution for this situation, we consider as a reference solution, the symmetric stress jump experiment reported by Jeffrey and Bunger [15]. In order to be able to compare the numerical solution to the

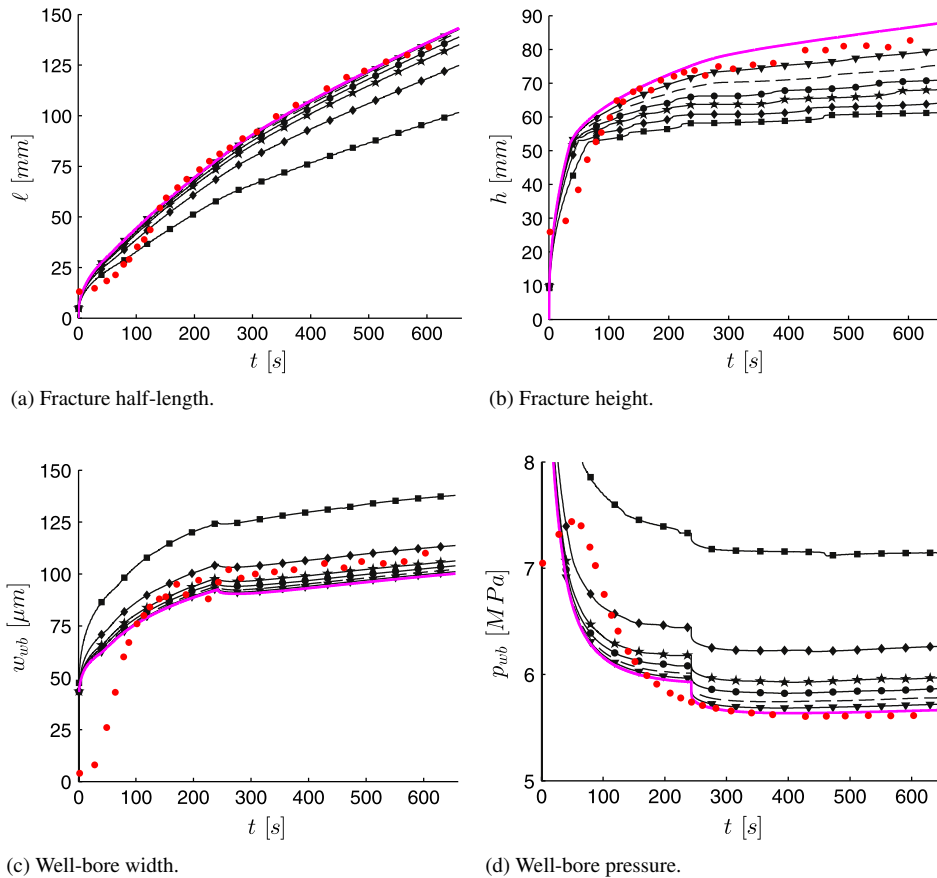


Fig. 7. Time evolution of the fracture half-length  $\ell$ , height  $h$ , well-bore width  $w_{wb}$ , and well bore pressure  $p_{wb}$ . The red solid circles denote the experimental results, which should be compared to ILSA M-Vertex solution denoted by the thick solid magenta line. The ILSA MK solutions, corresponding to the different toughness values  $K'$  (in  $\text{MPa m}^{1/2}$ ) are represented by thin black lines with the following symbols:  $\blacktriangledown$ — $K' = 0.75$ , dashed line— $K' = 1.0$ ,  $\bullet$ — $K' = 1.25$ ,  $\star$ — $K' = 1.5$ ,  $\blacklozenge$ — $K' = 2$ , and  $\blacksquare$ — $K' = 3$ .

experimental results, we assume the same parameter values as those reported for the experiment: Young’s modulus  $E = 3.3 \text{ MPa}$ , Poisson’s ratio  $\nu = 0.4$ , fluid viscosity  $\mu = 30.2 \text{ Pa s}$ , nominal injection rate  $Q_0 = 0.0017 \text{ ml/s}$ , payzone height  $H = 50 \text{ mm}$ , stress in the payzone  $\sigma_p = 2.2 \text{ MPa}$ , stress in the barrier zones  $\sigma_b = 6.5 \text{ MPa}$ , and stress jump  $\Delta\sigma = \sigma_b - \sigma_p = 4.3 \text{ MPa}$ . Due to fluid compressibility effects early in the experiment, the following two-stage injection schedule has been recommended [15]:

$$Q_0 = \begin{cases} 0.0020 \text{ ml/s} & \text{for } 0 < t \leq 243 \text{ s} \\ 0.0013 \text{ ml/s} & \text{for } 243 \text{ s} < t. \end{cases} \tag{5.2}$$

This experiment was simulated using ILSA in which the leading order term in the viscous asymptote (3.23) is used to locate the free boundary. A fine spatial mesh was used in which the 50 mm payzone was divided into 41 elements, so that  $\Delta x = \Delta y = 1.2195 \text{ mm}$  while a constant time step  $\Delta t = 0.2620 \text{ s}$  was used throughout the simulation. In the experiment the two sides of the “fracture plane”, in which the hydraulic fracture developed, were pushed together by flat jacks but were not bonded together, thus the experimental results correspond to the zero toughness M-vertex solution.

Plots of the fracture half-length, height, well-bore width, and well-bore pressure vs time for the experiment and the M-Vertex solution are shown in Fig. 7. For  $t > 250 \text{ s}$ , the ILSA M-vertex solution, represented by the thick line (colored magenta online), shows close agreement to the experimental results, represented by the isolated sequence of dots (colored red online). The initial discrepancies between the two sets of results stem largely from the fact that the numerical solution assumes a point source (having a log singularity in the pressure field) whereas a finite injection tube was used in the experiment, which naturally has a finite well-bore pressure. This initial discrepancy can also be

seen by the time that two fractures take to reach the stress barriers: the experimental fracture takes 74 s to achieve a fracture radius of 25 mm while the numerical solution takes 32 s.

If the two sides of the fracture plane were bonded together then the fracture toughness implied by this bond needs to be taken into account. Because different parts of the fracture boundary will be moving at different speeds, the fracture may evolve in such a way that one part of the boundary is advancing in the viscosity dominated regime while another part of the boundary is advancing in the toughness dominated regime. Between these extremes, it is also possible that for some time the fracture boundary may be advancing according to some intermediate asymptote as shown in Fig. 2. In order to be able to capture this multi-scale behavior it is necessary to use the ILSA-MK scheme described in Section 4.2. Assuming the same mesh and time step as before, the ILSA-MK scheme was used to simulate the same experiment multiple times in each case assuming that the two sides of the fracture plane are bonded and have one of the following scaled toughness values  $K' = [0.25, 0.5, 0.75, 1.0, 1.25, 1.5, 2, 2.5, 3, 3.5]$ . The results of some of these simulations are also plotted in Fig. 7. To be able to make more general conclusions, independent of the specific stress jump or payzone height, we use the dimensionless toughness  $\mathcal{K}_\sigma$  defined in [16]:

$$\mathcal{K}_\sigma = \sqrt{\frac{2\pi}{H} \frac{K_{Ic}}{\Delta\sigma}}. \quad (5.3)$$

Using the experimental values for the payzone height  $H$  and the stress jump  $\Delta\sigma$ , the values of the dimensionless toughness  $\mathcal{K}_\sigma$  corresponding the above sequence of values of  $K'$  are as follows:

$$\mathcal{K}_\sigma = [0.20, 0.41, 0.61, 0.82, 1.02, 1.23, 1.63, 2.04, 2.45, 2.86].$$

It can be seen that for moderate values of the dimensionless toughness in the range  $\mathcal{K}_\sigma \leq 1$  the presence of toughness has little impact on the half-length  $\ell$ , the well-bore width  $w_{wb}$ , and the well-bore pressure  $p_{wb}$ , but has a noticeable effect of on the height growth  $h$ .

In Fig. 8 we plot the spatial distributions of the ILSA M-vertex solution for the width and pressure fields at a selection of time steps within horizontal and vertical cross sections through the injection point. The smallest sample time  $t = 32.12$  s corresponds to the time at which the hydraulic fracture crosses the stress jump, while the largest sample time  $t = 603$  s corresponds to the last time for which experimental data is provided in [15]. We observe that the  $y$  cross section of the pressure field varies considerably initially ( $\infty$  at the well-bore to  $-\infty$  at the fracture front) but as time progresses the pressure field flattens appreciably. However, the vertical cross section of the pressure field is still not constant, which will be seen to have a significant impact on the accuracy of the P3D solution in this regime.

In Fig. 9, we plot the spatial distributions of the ILSA-MK solution for the width and pressure fields assuming  $K' = 1.25$  MPa  $m^{1/2}$  (or  $\mathcal{K}_\sigma = 1.02$ ). Comparing Figs. 8 and 9, we observe that, due to the toughness, the crossing time is delayed slightly to  $t = 35.26$  s, the fracture half length  $\ell$  is reduced slightly, while the fracture height is reduced significantly. This is consistent with the results shown in Fig. 7. The vertical cross section of the pressure field at later times is even flatter.

In Fig. 10 we plot the spatial distributions of the ILSA-MK solution for the width and pressure fields assuming  $K' = 1.5$  MPa  $m^{1/2}$  (or  $\mathcal{K}_\sigma = 1.23$ ). Comparing Figs. 8 and 10, we observe that, due to the toughness, the crossing time is delayed slightly to  $t = 37.36$  s, the fracture half length  $\ell$  is reduced somewhat more, while the fracture height is also reduced significantly.

In Fig. 11 we plot the fracture footprints at  $t = 32$  s of the M-vertex solution along with the footprints for the following values of the dimensionless toughness  $K' = 0.75, 1.25, \text{ and } 1.5$  MPa  $m^{1/2}$ . Only the first quadrant is shown due to the symmetry of the problem. This particular time has been chosen as it corresponds to the time at which the M-vertex solution breaks through the stress barrier and before which the solutions are all radially symmetric. Since the toughness retards the progress of the fracture, in each case the M-vertex footprint encompasses the MK footprint sampled at the corresponding time. In each case the ribbon of elements used to locate the MK free boundary (see Section 4.2) is shaded by the dominant length scale from the universal asymptote  $\hat{\xi}$  (see Fig. 2) that is active in that element. From Fig. 11 (a) we observe that when  $K' = 0.75$  MPa  $m^{1/2}$  there is very little difference between the M-vertex and the MK front positions. This is corroborated by the fact that, in this case, the all the ribbon elements for the MK solution are associated with a length scale  $\hat{\xi} \approx 10^{-1.5}$ , which according to Fig. 2, is still very close to the viscous regime. As further evidence that at this time, even with this non-zero toughness, the progress of this fracture is dominated by viscous propagation, the transition time for a radial MK solution in this case is  $t_{mk} = 686.26$  s (see

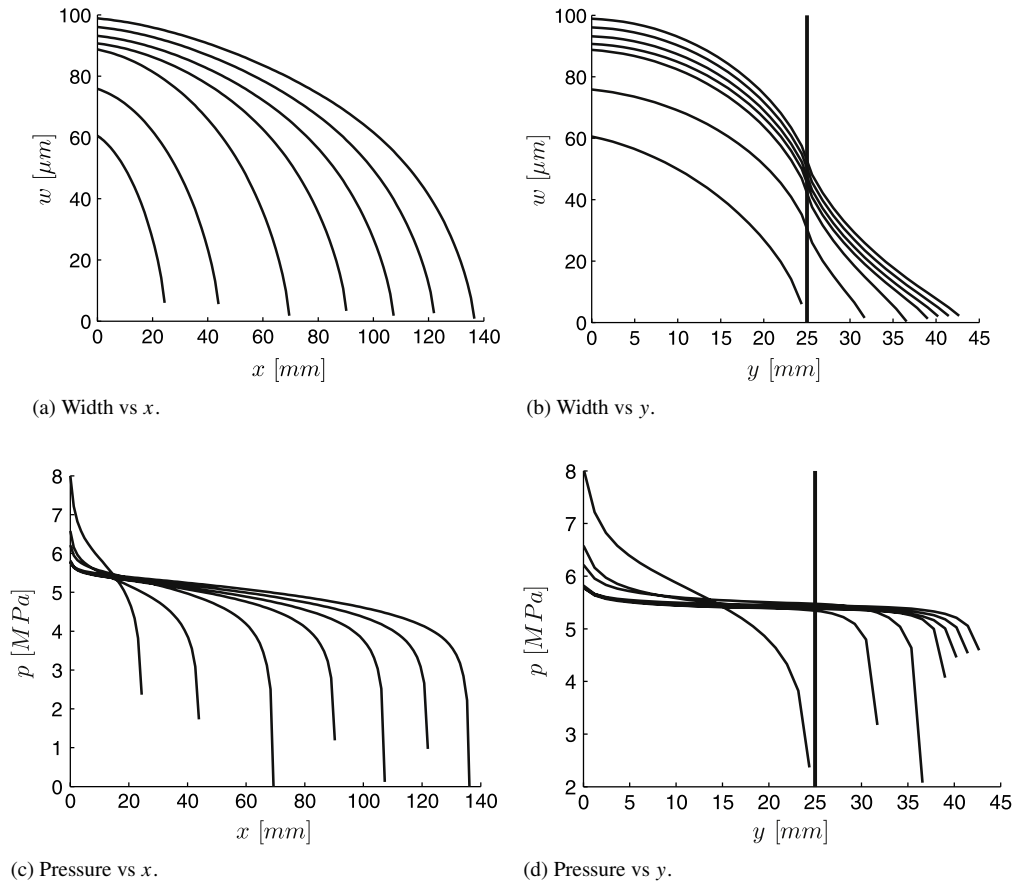


Fig. 8. Horizontal ( $x$ ) and vertical ( $y$ ) cross sections of the width and pressure fields for the M-vertex solution sampled at times  $t = 32.12, 100, 200, 300, 400, 500, 603$  s. The solid vertical lines in the vertical plots represent the interface across which the confining stress jumps.

Eq. (3.11)). Assuming  $K' = 1.25 \text{ MPa m}^{1/2}$  the MK and M-vertex footprints shown in Fig. 11(b) are now distinct, while the length scale in the ribbon elements is  $\hat{\xi} \approx 10^{-2.5}$ . The corresponding transition time in this case is  $t_{mk} = 6.92$  s so the MK radial fracture is well into the intermediate asymptotic regime. Assuming  $K' = 1.5 \text{ MPa m}^{1/2}$ , the MK and M-vertex footprints shown in Fig. 11(c) are now even further apart, while the length scale in the ribbon elements is  $\hat{\xi} \approx 10^{-3.5}$ . The corresponding transition time in this case is  $t_{mk} = 1.34$  s so the MK radial fracture is still in the intermediate asymptotic regime, but starting to move toward the toughness regime.

In Fig. 12 we plot the fracture footprint at  $t = 603$  s for the M-vertex solution along with the MK footprints for the following values of the scaled toughness  $K' = 0.75, 1.25, \text{ and } 1.5 \text{ MPa m}^{1/2}$ . In all cases it can be seen that the mode of propagation for the lateral wings of the fracture, whose dominant normal velocity component is horizontal, is different from the mode of propagation from those parts of the front whose dominant normal velocity component is vertical. This difference is more pronounced for smaller compared to larger values of the fracture toughness. From Fig. 12 (a) we observe that when  $K' = 0.75 \text{ MPa m}^{1/2}$ , that part of the fracture front within the payzone, for which the dominant component of the normal velocity field is horizontal, is associated with a length scale  $\hat{\xi} \approx 10^{-1.5}$ , which, according to Fig. 2, is still very much in the viscosity dominated regime. In this region the M-vertex and MK fracture front positions are very close. By contrast, that part of the fracture front beyond the interface is associated with a length scale  $\hat{\xi} \approx 10^{-4}$ , which is close to the toughness dominated regime. In this region the M-vertex and MK fracture front positions show a noticeable discrepancy, which results in the significantly different height growth shown in Fig. 7 (b). In Fig. 12 (b) and (c) all points along the boundary are associated with length scales  $\hat{\xi} \approx 10^{-4}$  or smaller, so that the fracture is propagating in the toughness dominated regime. In both these cases, due to the influence of the toughness, the MK footprints have significantly smaller half-lengths and heights.

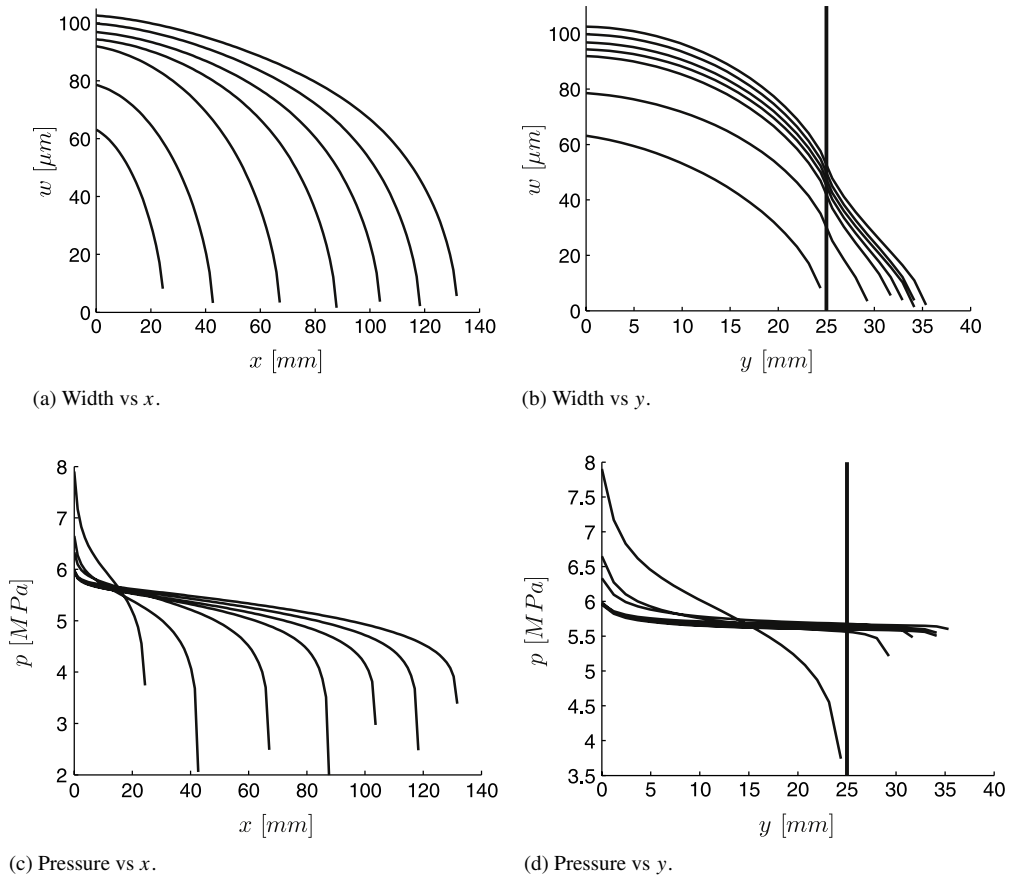


Fig. 9. Horizontal ( $x$ ) and vertical ( $y$ ) cross sections of the width and pressure fields assuming  $K' = 1.25 \text{ MPa m}^{1/2}$  (or  $\mathcal{K}_\sigma = 1.02$ ) sampled at times  $t = 35.26, 100, 200, 300, 400, 500, 603 \text{ s}$ . The solid vertical lines in the vertical plots represent the interface across which the confining stress jumps.

The scaled fracture half-length  $\ell/H$  and height growth  $\lambda = h/H$  values at times  $t = 603 \text{ s}$  and  $1048.5 \text{ s}$  are sampled for different values of the dimensionless toughness  $\mathcal{K}_\sigma$  and plotted in Fig. 13. As was observed in Fig. 7, for values of  $\mathcal{K}_\sigma < 1$  the fracture lengths do not vary much whereas the fracture height values change considerably over this interval. For  $\mathcal{K}_\sigma > 1$ , the effect of the fracture toughness starts to significantly reduce the fracture half-length, which decreases monotonically as  $\mathcal{K}_\sigma$  increases. As expected, initially the height growth also decreases with increasing  $\mathcal{K}_\sigma$ . However, a value of  $\mathcal{K}_\sigma$  is reached at which the height growth achieves minimum value and beyond which it is easier for the fracture to grow vertically rather than horizontally.

### 5.2.2. Comparison to an equilibrium P3D model

As the aspect ratio  $h/2\ell$  of these blade-like fractures decreases, a condition close to a state plane strain starts to develop in any vertical cross section located away from the fracture tips. Thus, once the aspect ratio is sufficiently small, vertical cross sections of the ILSA-MK solutions can be compared to the solutions for a plane strain crack subject to a prescribed pressure field. Indeed, these plane strain solutions form the basic building blocks for so-called P3D models that are specifically designed to approximate symmetric stress jump configurations such as the one shown in Fig. 6. The objective of this section is to try to validate the ILSA-MK model by comparing vertical cross-sections of the ILSA-MK solutions to the analytic solution for a pressurized plane strain crack. In addition, we take the opportunity to compare the ILSA-MK solutions to the corresponding P3D model solutions. This comparison helps to establish the regions of applicability of the P3D model as well as exposes some of its deficiencies, which can be linked directly to the underlying assumptions of the P3D model.

In this comparison we make use of the P3D formulation and scalings presented in [16]. In order to discuss the discrepancies between the P3D results and the experimental and ILSA results, it is important to summarize the three

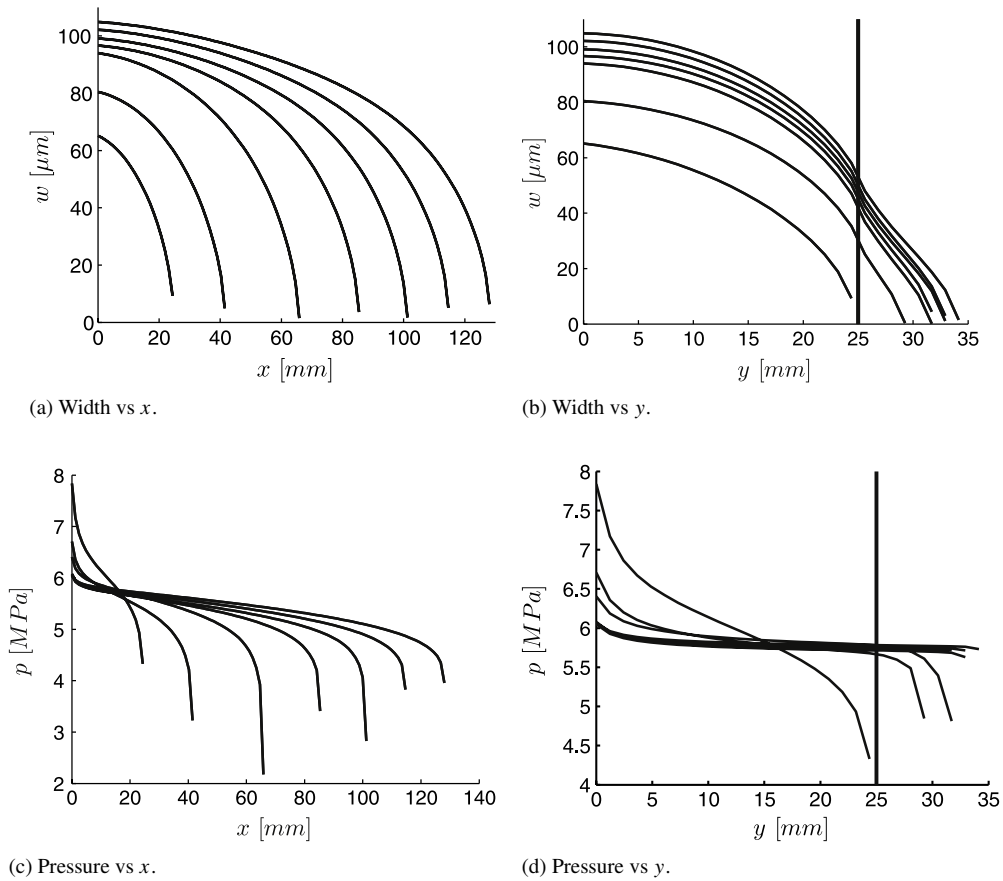


Fig. 10. Horizontal ( $x$ ) and vertical ( $y$ ) cross sections of the width and pressure fields assuming  $K' = 1.5 \text{ MPa m}^{1/2}$  (or  $\mathcal{K}_\sigma = 1.23$ ) sampled at times  $t = 37.36, 100, 200, 300, 400, 500, 603 \text{ s}$ . The solid vertical lines in the vertical plots represent the interface across which the confining stress jumps.

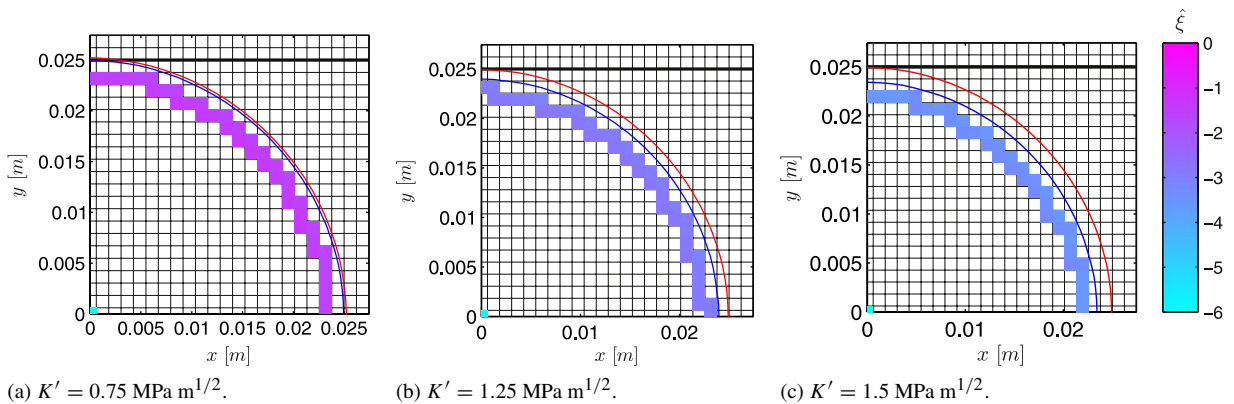


Fig. 11. Fracture footprints  $C(t)$  at time  $t = 32 \text{ s}$  for different values of the fracture toughness. In each of the figures, the M-vertex footprint (shown red online) encompasses the MK footprint (shown blue online), which is sampled at the corresponding time. The DD mesh is denoted by the thin grid lines and the thick horizontal lines represent the interface across which the confining stress field jumps. The length scale  $\hat{\xi}$  active in locating the free boundary is depicted by the shaded elements. (For interpretation of the references to color in this figure legend, the reader is referred to the web version of this article.)

basic assumptions used in the P3D model for an impermeable rock-mass, which are as follows: (I) The lateral wings of the fracture are vertical and restricted to the pay zone; (II) the vertical fluid flux is sufficiently small that the fluid

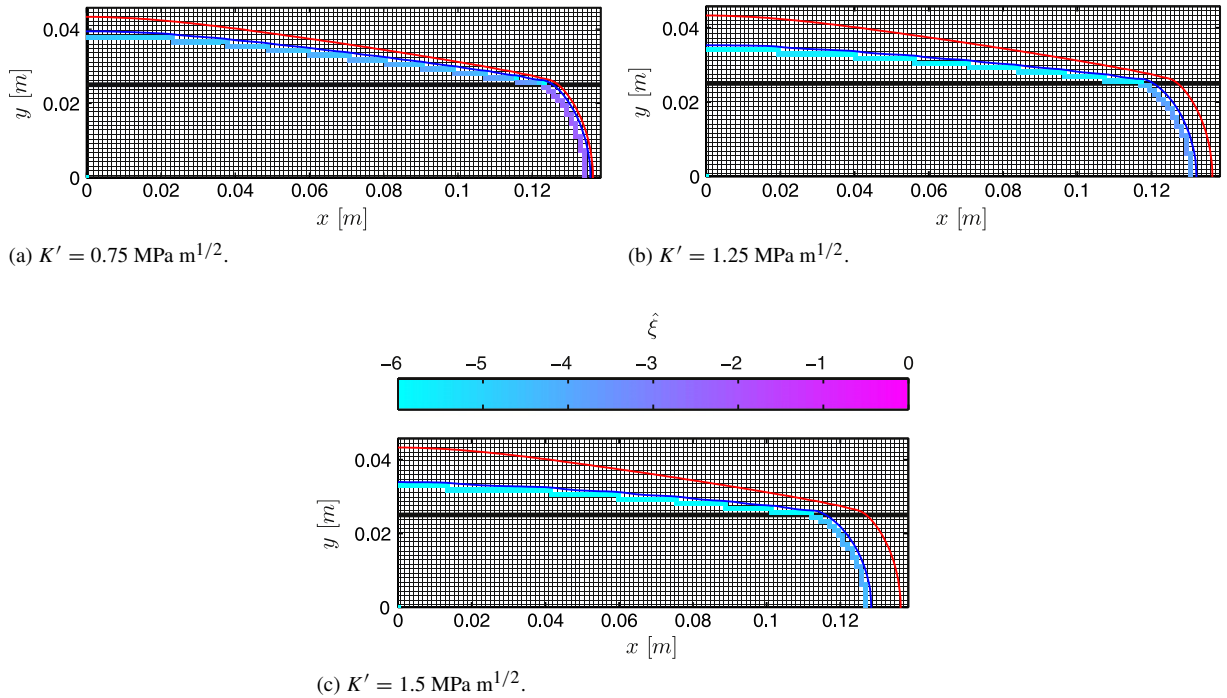


Fig. 12. Fracture footprints  $C(t)$  at time  $t = 603 \text{ s}$  for different values of the fracture toughness.

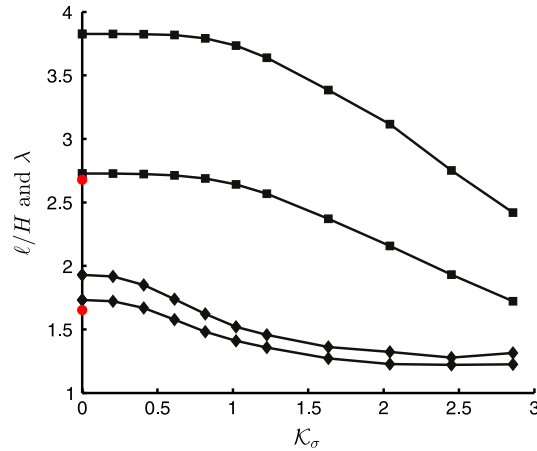


Fig. 13. The scaled fracture half-lengths  $\ell/H$  (■) and fracture heights  $\lambda = h/H$  (◆) sampled at times  $t = 603 \text{ s}$  and  $1048.5 \text{ s}$  and plotted as a function of  $\mathcal{K}_\sigma$ . The solid circles (colored red online) represent the experimental scaled half-length and height.

pressure  $p_f$  can be considered constant in any vertical plane; (III) The aspect ratio  $h/2\ell$  is sufficiently small that a condition of plane strain exists in any vertical plane. The nonlocal elasticity equation can then be replaced by a local relation between the average width and the fluid pressure. This local assumption breaks down in the lateral leading edges of the fracture a distance  $O(H)$  from the tip, which precludes the imposition of any appropriate propagation condition. Instead, the kinematic condition  $w = 0$  (and therefore  $p_f = 0$ ) is imposed. Nonlocal corrections to this model in the case  $h = H$  can be found in [36].

Finally, we note that for this comparison we assume that fluid injection rate is  $Q_0 = 0.0017/\text{ml/s}$  throughout the simulations, otherwise we use precisely the same parameters as in the previous sub-section.

In Fig. 14 we plot the ILSA-MK and P3D scaled fracture half-lengths  $\ell/H$  and scaled heights  $\lambda = h/H$  sampled at time  $t = 603 \text{ s}$  versus the dimensionless toughness  $\mathcal{K}_\sigma$ . When  $\mathcal{K}_\sigma = 0$ , we observe that the P3D model grossly

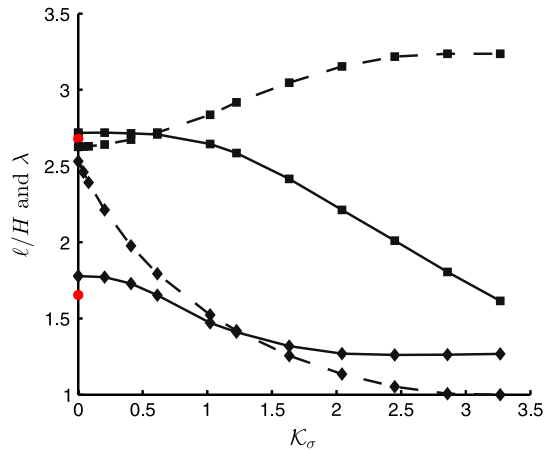


Fig. 14. The scaled fracture half-lengths  $\ell/H$  (■) and fracture heights  $\lambda = h/H$  (◆) sampled at time  $t = 603$  s and plotted as a function of  $\mathcal{K}_\sigma$  for both the ILSA-MK (solid lines) and P3D (dashed lines) models. The solid circles (colored red online) represent the experimental scaled half-length and height.

over-estimates the height growth registered by the experiment and the ILSA scheme, but provides a good estimate of the fracture half-length  $\ell$ . The poor height growth estimate of the P3D model is largely due to the assumption of a constant fluid pressure  $p_f$  in the vertical direction used in the P3D model, which is clearly not valid as can be seen from Fig. 8(d). The P3D fracture half-length shows good agreement with the ILSA model and the experiment, which is consistent with the fact that the fracture half-length  $\ell$  is determined largely by viscous dissipation over the length of the fracture and conservation of fluid volume. The initial height-growth error in the P3D model decreases as  $\mathcal{K}_\sigma$  is increased but is still significant in the range  $0 < \mathcal{K}_\sigma < 1/2$ . As  $\mathcal{K}_\sigma$  is increased, the pressure variation in the vertical direction (and therefore the fluid flux  $q_y$ ) is decreased sufficiently for the P3D Assumption I – of constant pressure in vertical cross-sections – to become valid. Indeed, for  $1/2 < \mathcal{K}_\sigma < 2$  the P3D model gives reasonable height growth estimates that are within 10% of the ILSA-MK solution. For  $0 \leq \mathcal{K}_\sigma < 1$  the P3D model provides an estimate of the fracture length that is also within 10% of the ILSA-MK, since within this range the ILSA-MK fracture length is almost identical to that of the M-vertex solution, and is influenced very little by the toughness. Recall that the P3D model cannot account for toughness in the propagation of the lateral wings of the fracture, while it does account for toughness in determining the vertical height growth. Thus in the P3D model, since increasing  $\mathcal{K}_\sigma$  offers no additional resistance to lateral growth of the fracture, while it does place increased restriction on the vertical height growth, conservation of fluid volume dictates that the P3D length estimate must increase with increasing  $\mathcal{K}_\sigma$  until the toughness is so large that  $h = H$  and  $\ell$  no longer increases with  $\mathcal{K}_\sigma$ . In contrast, for  $\mathcal{K}_\sigma > 1$ , the ILSA-MK half-length  $\ell$  decreases monotonically with increasing  $\mathcal{K}_\sigma$ .

Assuming a constant fluid pressure  $p_f$  in any vertical cross section, the following expression relating the scaled fluid pressure  $\Pi_f = \frac{p_f}{\Delta\sigma}$ , the dimensionless toughness  $\mathcal{K}_\sigma$ , and the scaled height growth  $\lambda = h/H$  can be derived [16]:

$$\Pi_f = \frac{\mathcal{K}_\sigma}{\pi\sqrt{\lambda}} + \frac{\sigma_b}{\Delta\sigma} - \frac{2}{\pi} \sin^{-1}\left(\frac{1}{\lambda}\right). \tag{5.4}$$

In Fig. 15 we plot, as functions of  $\lambda$ , the P3D pressure  $\Pi_f$  given by (5.4) as well as the ILSA-MK well-bore pressure for the cases  $\mathcal{K}_\sigma = 0, 1.02$ , and  $2.04$ . For the case  $\mathcal{K}_\sigma = 0$  we also plot the corresponding experimental well-bore pressures as a function of  $\lambda$ . From Fig. 7(b) we observe that, since  $h$  is a monotonically increasing function of  $t$ , we can regard  $\lambda$  in Fig. 15 as a proxy for time. Thus initially the well-bore pressures for the ILSA-MK solutions as well as the experiment are decreasing with time as is characteristic of a radially symmetric solution. However, as the fracture aspect ratio decreases, the well-bore pressures reach a minimum (at  $\lambda = 1.56$  for  $\mathcal{K}_\sigma = 0$ ,  $\lambda = 1.31$  for  $\mathcal{K}_\sigma = 1.02$ , and  $\lambda = 1.21$  for  $\mathcal{K}_\sigma = 2.04$ ), and, for the larger toughness values, the well-bore pressures asymptote to just above the increasing P3D pressures. Because the ILSA-MK solution approximates a log singularity, due to the point source model of the well-bore, it is to be expected that the ILSA well-bore pressures should be slightly higher than the P3D pressures, which represent the average pressure over each vertical plane (see Figs. 8(d)–10(d)). For the zero toughness case, the last solid circle, the solid square, and the ★ symbol represent the experimental,

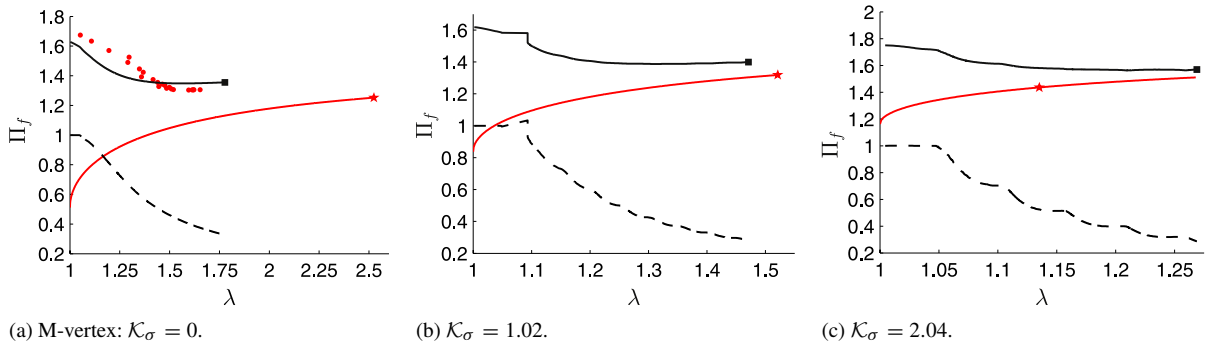


Fig. 15. The ILSA-MK well-bore pressures vs  $\lambda$  represented by the solid curve (black online) terminated by a  $\blacksquare$  symbol and the corresponding P3D  $\Pi_f$  vs  $\lambda$  from Eq. (5.4) represented by the solid curve (colored red online) with a solid  $\star$  symbol. For the M-vertex case  $\mathcal{K}_\sigma = 0$ , the experimental results are represented by the solid circles (red online). The dashed line in each case represents the aspect ratio  $h/2\ell$  for the ILSA-MK solution.

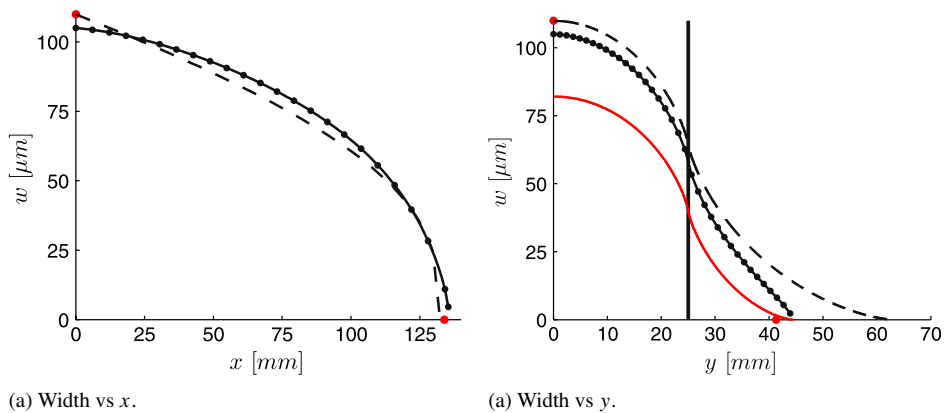


Fig. 16. Horizontal ( $x$ ) and vertical ( $y$ ) cross sections of the width and pressure fields for the M-vertex case  $\mathcal{K}_\sigma = 0$  sampled at time  $t = 603$  s. The solid vertical line in the vertical plot represents the interface across which the confining stress jumps. The ILSA-MK widths are represented by the solid lines with the  $\bullet$  symbols, while the corresponding P3D solutions are represented by dashed lines.

ILSA-MK, and the P3D values corresponding to time  $t = 603$  s, respectively. There is a large difference between the pair  $(\lambda, \Pi_f)$  for P3D and the corresponding experimental and ILSA-MK pairs, which are relatively close. For the case  $\mathcal{K}_\sigma = 1.02$  the corresponding  $(\lambda, \Pi_f)$  pairs for the ILSA-MK ( $\blacksquare$ ) and P3D ( $\star$ ) solutions are relatively close, which is consistent with the reasonably accurate P3D height estimate if  $\mathcal{K}_\sigma \approx 1$ . When  $\mathcal{K}_\sigma = 2.04$  the ILSA-MK ( $\blacksquare$ ) and P3D ( $\star$ ) solutions start to diverge significantly even though the ILSA-MK well-bore pressures are approaching the P3D pressures asymptotically for increasing  $\lambda$ . This is due to the poor estimate of  $\lambda$  for the P3D solution because the P3D solution does not account for toughness in its lateral wings and therefore grossly over-estimates the fracture half-length  $\ell$ . Fluid volume conservation therefore dictates that the P3D  $\lambda$  values will be too small.

Introducing the following scalings  $h = H\lambda$ ,  $y = H\zeta$ ,  $w = w_*\Omega$ , where  $w_* = \frac{\pi H \Delta\sigma}{2E'}$ , and assuming a constant pressure for vertical cross sections and that conditions of plane strain prevail, it follows [16] that for  $|\zeta| < \lambda/2$  and  $\zeta \neq 1/2$  the scaled fracture opening can be written as:

$$\Omega(\zeta, \lambda) = \frac{8}{\pi^2} \left\{ \frac{\mathcal{K}_\sigma}{2\sqrt{\lambda}} \sqrt{\lambda^2 - 4\zeta^2} - \varsigma \log \left| \frac{\sqrt{\lambda^2 - 4\zeta^2} + 2\zeta\sqrt{\lambda^2 - 1}}{\sqrt{\lambda^2 - 4\zeta^2} - 2\zeta\sqrt{\lambda^2 - 1}} \right| + \frac{1}{2} \log \left| \frac{\sqrt{\lambda^2 - 4\zeta^2} + \sqrt{\lambda^2 - 1}}{\sqrt{\lambda^2 - 4\zeta^2} - \sqrt{\lambda^2 - 1}} \right| \right\} \tag{5.5}$$

and when  $\zeta = 1/2$  the last two terms in (5.5) should be replaced by  $-\log\left(\frac{1}{\lambda}\right)$ .

In Fig. 16, we compare the ILSA-MK and P3D horizontal and vertical width cross sections for the M-vertex case  $\mathcal{K}_\sigma = 0$  sampled at time  $t = 603$  s. The isolated solid circles (colored red online) plotted along the axes represent the corresponding height, half-length, and width results measured in the experiment. In plot (b) the solid curve without

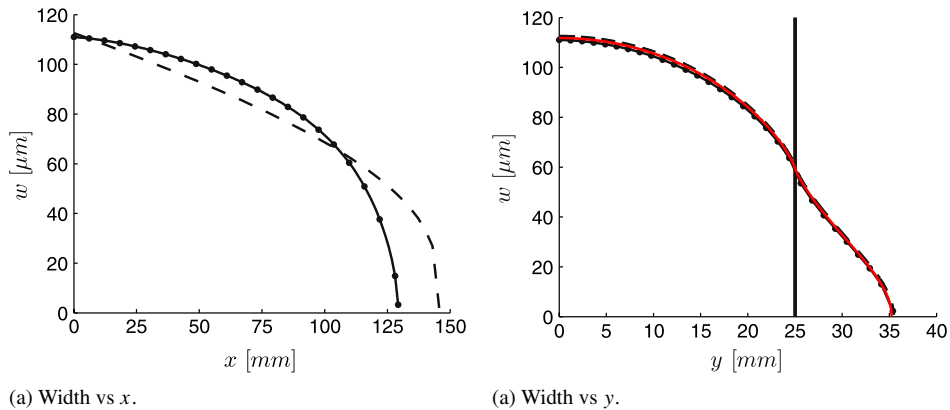


Fig. 17. Horizontal ( $x$ ) and vertical ( $y$ ) cross sections of the width and pressure fields for the case  $\mathcal{K}_\sigma = 1.23$  sampled at time  $t = 603$  s. The solid vertical line in the vertical plot represents the interface across which the confining stress jumps. The ILSA-MK widths are represented by the solid lines with the  $\bullet$  symbols, while the corresponding P3D solutions are represented by the dashed curves.

symbols (colored red online) represents the width profile given by (5.5) assuming the ILSA-MK  $\lambda$  value. We observe from Fig. 16(a) that the ILSA-MK and P3D horizontal cross sections of the width and the fracture half-lengths show close agreement in this case, both of which agree with the experimental well-bore widths and fracture half-lengths. This close agreement is due to the fact that the fracture length, in this case, is largely determined by the viscous dissipation that takes place over the length of the fracture, which is largely the same for the two models. We observe from Fig. 16(b) that the vertical cross sections of the ILSA-MK and P3D widths have similar maximum values but within the stress barrier ( $y > 25$  mm) the two solutions show a significant difference. This is largely due to over-estimation of the fracture height  $h$  by the P3D model as it assumes a constant pressure field rather than the decreasing pressure field characteristic of the ILSA-MK (see Fig. 8(d)). We note the close agreement between the ILSA-MK well-bore width and height and the corresponding experimental values, which are depicted by the isolated solid circles (shown red online) plotted on the axes.

In Fig. 17, we compare the ILSA-MK and P3D horizontal and vertical width cross sections for the case  $\mathcal{K}_\sigma = 1.23$  sampled at time  $t = 603$  s. We observe from Fig. 17(a) that the ILSA-MK and P3D horizontal cross sections of the width and the fracture half-lengths are markedly different in this case. This difference is due to the fact that the fracture toughness has a significant impact on the ILSA-MK solution, whereas the P3D lateral growth cannot account for toughness and is largely determined by viscous dissipation. As before, in Fig. 17(b) the solid curve without symbols (colored red online) represents the width profile given by (5.5) assuming the ILSA-MK  $\lambda$  value. The close agreement between the width profile given by (5.5) and that given by the ILSA-MK scheme, indicates that the blade-like fracture has moved into a regime in which a state of plane strain prevails in vertical cross sections and the pressure field is almost constant. This close agreement also indicates that the ILSA-MK scheme estimates the fracture width and fracture height  $h$  accurately. For the ILSA-MK scheme, nothing is particularly special about this particular sample time, except that the fracture footprint has evolved sufficiently for the plane strain condition and near constant pressure to hold in vertical cross sections, which makes a comparison with an analytic solution possible. From this comparison we are thus able to get an idea about the accuracy with which the ILSA-MK scheme is able to capture the fracture width  $w$  and estimate the fracture height  $h$ . Moreover, since the ILSA-MK scheme uses precisely the same logic to determine the fracture length (or any point along the fracture boundary for that matter), it seems reasonable to expect that the ILSA-MK scheme is able to provide similar orders of accuracy throughout the simulation time. We observe from this figure that the vertical cross sections of the ILSA-MK and P3D schemes also show extremely good agreement. This is partly due to the fact that plane strain and near constant pressure conditions hold in vertical cross sections, and the fact that the P3D over-estimate of the fracture length is partially compensated for by a corresponding under-estimate of the fracture widths between the well-bore and the tip. There is a significant decrease in the variation of the ILSA-MK pressure field that can be seen from Fig. 10(d), which implies that the assumption of a constant fluid pressure in vertical cross sections used in the P3D model is a good approximation in this case.

In Fig. 18, we compare the ILSA-MK and P3D horizontal and vertical width cross sections for the case  $\mathcal{K}_\sigma = 2.04$  sampled at time  $t = 603$  s. We observe from Fig. 18(a) that the ILSA-MK and P3D horizontal cross sections of the

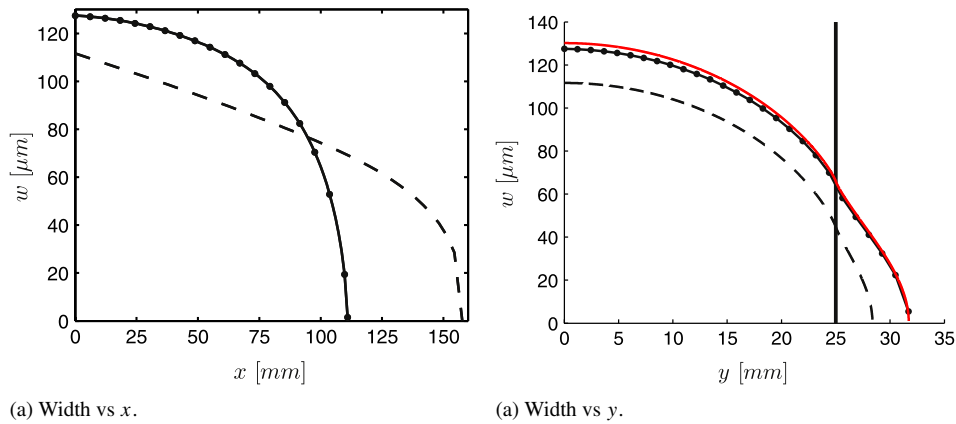


Fig. 18. Horizontal ( $x$ ) and vertical ( $y$ ) cross sections of the width and pressure fields for the case  $\mathcal{K}_\sigma = 2.04$  sampled at time  $t = 603$  s. The solid vertical line in the vertical plot represents the interface across which the confining stress jumps. The ILSA-MK widths are represented by the solid lines with the  $\bullet$  symbols, while the corresponding P3D solutions are represented by the dashed curves.

width and the fracture half-lengths are significantly different in this case. The fracture toughness has a large impact on the ILSA-MK solution, whereas the P3D lateral growth is still determined by viscous dissipation. From Fig. 18(b) we also observe that there is a significant difference between the ILSA-MK and P3D solutions, due to the poor estimation of the fracture height by the P3D solution. This poor P3D height estimate is due to the significantly different distribution of the fluid volumes in the P3D and ILSA-MK solutions, because the P3D solution significantly over-estimates the fracture half-length. The solid curve without symbols (colored red online) representing the width profile given by (5.5) assuming the ILSA-MK  $\lambda$  value, is slightly larger than the ILSA-MK solution. Comparing Figs. 18(b) and 17(b), it is surprising that there is a larger discrepancy in the case with a larger toughness, because the fluid pressure in vertical cross-sections, if anything, can be expected to vary even less in this case. This discrepancy, is likely due to the fact that the aspect ratios are different in these two situations, which impacts the assumption of a condition of plain strain in vertical cross sections used to derive (5.5). However, despite this slight discrepancy, the close agreement between the ILSA-MK width field and that given by (5.5) indicates that the ILSA-MK scheme provides an accurate estimate of the field variables.

## 6. Conclusions

It is well established that hydraulic fractures often involve the competition between multiple physical processes, which manifest themselves at multiple length scales and on multiple time scales [5]. Accurately capturing such multi-scale behavior, which typically involves length scale variations of 6–8 orders of magnitude, using reasonably modest computational resources poses significant challenges for the numerical modeler. Setting the mesh size to the finest active length scale would resolve the problem, however this approach would require so many computing resources and so much CPU time that it is impracticable. On the other hand, adapting the mesh to the constantly changing length scale of the dominant physical process is also a daunting task—particularly in the context of the singular free boundary problems typically encountered when modeling hydraulic fracture propagation.

To resolve this multi-scale problem, we have developed an implicit level set algorithm (ILSA) [11] suitable for capturing the multi-scale behavior typically encountered when modeling propagating hydraulic fractures that involve multiple competing physical processes. In this paper we have illustrated this formulation for two competing dissipative processes one associated with viscosity involving viscous dissipation and the other with fracture toughness involving the fracture energy required to break the rock. The key component in this algorithm is a universal solution [13] for a semi infinite hydraulic fracture propagating in a state of plane strain. This solution connects the classic LFM  $O(\xi^{1/2})$  behavior [28] close to the fracture tip associated with the toughness, with the  $O(\xi^{2/3})$  behavior [7] at infinity, which is associated with viscous dissipation. Between these extremes this solution captures all the intermediate behavior in which the two competing physical processes contribute to a varying degree. The methodology outlined here can also be used to model more than two competing physical processes. For example, if, in addition to viscosity and toughness, we need to model a third physical process such as Carter leak-off into the reservoir, the appropriate

generalized asymptote [30] needs to be used. In this paper, we have chosen to focus on these two competing processes so that we can demonstrate efficacy of the new multi-scale algorithm in a regime for which there is a published reference solution and whose solutions can be compared to experimental results. We defer the implementation of three or more competing processes for further research.

The ILSA-MK scheme uses an appropriate mapping procedure, based on the local front velocity, to identify the dominant length scale at which the semi infinite solution should be sampled in order to locate the unknown free boundary. Moreover, by integrating the semi infinite solution over tip elements, the ILSA-MK scheme is able to capture, *in a weak sense*, all the finer-scale structure of the solution between the current dominant length scale and the tip. Having matched current dominant length scale to the mesh size, the ILSA-MK scheme is also able to capture all the coarser-scale behavior of the finite fracture. Thus by dynamically adjusting the dominant length scale the ILSA-MK algorithm is able to represent, on a relatively coarse rectangular mesh, all the length scales active in the problem, which can vary along the boundary of the fracture and with time.

We provide a comparison between the novel ILSA-MK solution and a reference solution [14], comprising a radial fracture evolving from a viscous dominated regime to a toughness dominated regime. The fracture radius evolution, fracture width and fluid pressure profiles of the ILSA-MK and reference solutions show very close agreement. To illustrate the capacity of the ILSA-MK scheme to model heterogeneous situations in which different parts of the fracture boundary can be propagating via different dominant physical processes, we considered a problem involving a symmetric stress jump, which is a typical situation encountered in hydraulic fracture treatments in the oil and gas industry. As a reference configuration we chose to consider the symmetric stress jump experiment reported by Jeffrey and Bungler [15]. This enabled the experimental results to be used as a reference solution for the zero toughness case  $K' = 0$ . The ILSA-MK solution showed close agreement with the experimental results in this case. The ILSA-MK scheme was used to generate solutions to non-zero toughness situations in which  $K' > 0$ . It is hoped that these solutions will be useful to establish the applicability of simulators that use a propagation criterion based on only one dissipative process (either toughness or viscosity). For advanced times, when the fracture has evolved sufficiently for a situation of plane strain to develop in vertical cross sections, the ILSA-MK solution was compared to the plane strain exact solutions for height growth and fracture width in such vertical cross sections. The ILSA-MK solutions showed close agreement with these exact solutions when they could be expected to agree. The ILSA-MK scheme was also used to establish the regimes of validity of the equilibrium P3D models, within which height growth and fracture length estimates are reliable. Moreover, it is also hoped that these benchmark results can also be used to design enhancements to P3D models that will improve their accuracy.

## Acknowledgments

The author gratefully acknowledges the grant support of NSERC (Canada). In addition, the author would like to thank Professors E. Detournay, (U. of Minnesota) and D. Garagash (Dalhousie U.), for providing the universal asymptotic solution in a numerical form; Dr. B. Lecampion for assistance in preparing the results of the radial reference solution; and Dr. E. Dontsov for assistance in preparing some of the P3D results.

## References

- [1] M.J. Economides, K.G. Nolte (Eds.), *Reservoir Stimulation*, John Wiley & Sons, Ltd., New York, 2000.
- [2] R.G. Jeffrey, K.W. Mills, Hydraulic fracturing applied to inducing longwall coal mine goaf falls, in: *Pacific Rocks 2000*, Balkema, Rotterdam, 2000, pp. 423–430.
- [3] A. van As, R.G. Jeffrey, Caving induced by hydraulic fracturing at North Parkes mines, in: *Pacific Rocks 2000*, Balkema, Rotterdam, 2000, pp.353–360.
- [4] J. Adachi, E. Siebrits, A. Peirce, J. Desroches, Computer simulation of hydraulic fractures, *Int. J. Rock Mech. Min. Syst.* 44 (5) (2007) 739–757.
- [5] E. Detournay, Propagation regimes of fluid-driven fractures in impermeable rocks, *Int. J. Geomech.* 4 (2004) 111.
- [6] D.A. Spence, P. Sharp, Self-similar solutions for elastohydro dynamic cavity flow, *Proc. R. Soc. Lond. Ser. A Math. Phys. Eng. Sci.* 400 (1985) 289–313.
- [7] J. Desroches, E. Detournay, B. Lenoach, P. Papanastasiou, J.R.A. Pearson, M. Thiercelin, A.H.D. Cheng, The Crack Tip Region in Hydraulic Fracturing, *Proc. R. Soc. Lond. Ser. A Math. Phys. Eng. Sci.* 447 (1994) 39–48.
- [8] J.I. Adachi, E. Detournay, Plane-strain propagation of a fluid-driven fracture in a permeable medium, *Eng. Fract. Mech.* 75 (2008) 4666–4694.
- [9] D.I. Garagash, Plane-strain propagation of a fluid-driven fracture during injection and shut-in: Asymptotics of large toughness, *Engineering Fracture Mech.* 73 (2006) 456–481.

- [10] S.L. Mitchell, R. Kuske, A.P. Peirce, An asymptotic framework for the analysis of hydraulic fractures: the impermeable case, *ASME J. Appl. Mech.* 74 (2) (2007) 365–372.
- [11] A. Peirce, E. Detournay, An implicit level set method for modeling hydraulically driven fractures, *Comput. Methods Appl. Mech.* 197 (2008) 2858–2885.
- [12] B. Lecampion, A.P. Peirce, E. Detournay, X. Zhang, Z. Chen, A.P. Bunger, C. Detournay, J. Napier, S. Abbas, D. Garagash, P. Cundall, The impact of the near-tip logic on the accuracy and convergence rate of hydraulic fracture simulators compared to reference solutions, in: A.P. Bunger, J. McLennan, R. Jeffrey (Eds.), *Effective and Sustainable Hydraulic Fracturing*, ISBN: 978-953-51-1137-5, 2013, pp. 855–873. (Intech), (Chapter 43).
- [13] D. Garagash, Near-tip processes of fluid-driven fractures (Ph.D. thesis), University of Minnesota, Minneapolis, 1998.
- [14] M. Madyarova, Fluid-driven penny-shaped fracture in permeable rock (Ph.D. thesis), University of Minnesota, 2003.
- [15] R.G. Jeffrey, A.P. Bunger, 2007. A detailed comparison of experimental and numerical data on hydraulic fracture growth through stress contrasts. In: *Proc. 2007 SPE Hydraulic Fracturing Technology Conference*, College Station, 29–31 Jan., 2007. Paper SPE 106030.
- [16] J.I. Adachi, E. Detournay, A. Peirce, An analysis of classical pseudo-3D model for hydraulic fracture with equilibrium height growth across stress barriers, *Int. J. Rock Mech. Min. Sci.* 47 (2010) 625–639.
- [17] E. Simonson, A. Abou-Sayed, R. Clifton, Containment of massive hydraulic fractures., *SPE JOURNAL* 18 (1) (1978) 27–32. [SPE 6089].
- [18] A. Settari, M.P. Cleary, Development and testing of a pseudo-three-dimensional model of hydraulic fracture geometry. *SPE Production Engineering*, November 1986. pp. 449–466.
- [19] M.G. Mack, R. Warpinski, Mechanics of hydraulic fracturing, in: M.J. Economides, K.G. Nolte (Eds.), *Reservoir Stimulation*, third ed., John Wiley & Sons, Chichester, UK, 2000 (Chapter 6).
- [20] D.I. Garagash, E. Detournay, The tip region of a fluid-driven fracture in an elastic medium, *ASME J. Appl. Mech.* 67 (1) (2000) 183–192.
- [21] A.P. Bunger, E. Detournay, Early time solution for a penny-shaped hydraulic fracture, *ASCE J. Engrg. Mech.* 133 (5) (2007) 175–190.
- [22] E. Detournay, A. Peirce, On the moving boundary conditions for a hydraulic fracture, *Int. J. Eng. Sci.* 84 (2014) 147–155.
- [23] A.P. Peirce, E. Siebrits, The scaled flexibility matrix method for the efficient solution of boundary value problems in 2D and 3D layered elastic media, *Comput. Methods Appl. Mech. Engrg.* 190 (2001) 5935–5956.
- [24] A.P. Peirce, E. Siebrits, Uniform asymptotic approximations for accurate modeling of cracks in layered elastic media, *Int. J. Fract.* 110 (2001) 205–239.
- [25] E. Siebrits, A.P. Peirce, An efficient multi-layer planar 3D fracture growth algorithm using a fixed mesh approach, *Int. J. Numer. Methods Engrg.* 53 (2002) 691–717.
- [26] S.L. Crouch, A.M. Starfield, *Boundary Element Methods in Solid Mechanics*, George Allen and Unwin, London, 1983.
- [27] D.A. Hills, P.A. Kelly, D.N. Dai, A.M. Korsunsky, *Solution of Crack Problems, The Distributed Dislocation Technique*, Solid Mechanics and its Applications, vol. 44, Kluwer Academic Publisher, Dordrecht, 1996.
- [28] J.R. Rice, in: H. Liebowitz (Ed.), *Mathematical Analysis in the Mechanics of Fracture*, Fracture, an Advanced Treatise, Academic Press, New York, 1968, pp. 191–311 (Chapter 3).
- [29] D.I. Garagash, E. Detournay, Plane-strain propagation of a fluid-driven fracture: small toughness solution, *ASME J. Appl. Mech.* 72 (2005) 916–928.
- [30] D. Garagash, E. Detournay, J. Adachi, Multi-scale tip asymptotics in hydraulic fracture with leak-off, *J. Fluid Mech.* 669 (2011) 260–297.
- [31] A. Peirce, Localized Jacobain ILU preconditioners for hydraulic fractures, *Internat. J. Numer. Methods Engrg.* 65 (12) (2006) 1935–1946.
- [32] A.P. Peirce, E. Siebrits, A dual mesh Multigrid preconditioner for the efficient solution of hydraulically driven fracture problems, *Internat. J. Numer. Methods Engrg.* 63 (13) (2005) 1797–1823.
- [33] J.A. Sethian, *Level Set Methods and Fast Marching Methods: Evolving Interfaces in Computational Geometry Fluid Mechanics Computer Vision and Materials Science*, Cambridge University Press, Cambridge, UK, 1999.
- [34] S. Osher, R. Fedkiw, Level set methods and dynamic implicit surfaces, in: *Applied Mathematical Sciences*, vol. 153, Springer-Verlag, New York, 2002.
- [35] A.A. Savitski, E. Detournay, Propagation of a fluid-driven pennyshaped fracture in an impermeable rock: asymptotic solutions, *Int. J. Solids Struct.* 39 (26) (2002) 6311–6337.
- [36] J. Adachi, A.P. Peirce, Asymptotic analysis of an elasticity equation for a finger-like hydraulic fracture, *J. Elasticity* 90 (2008) 43–69.